Submitted to Eur. Phys. J. **C**

Measurement of $D^{*\pm}$ production and the charm contribution to F_2 in deep inelastic scattering at HERA

ZEUS Collaboration

Abstract

The production of $D^{*\pm}(2010)$ mesons in deep inelastic scattering has been measured in the ZEUS detector at HERA using an integrated luminosity of 37 pb^{-1}. The decay channels $D^{*+} \to D^0\pi^+$ (+c.c.), with $D^0 \to K^-\pi^+$ or $D^0 \to K^-\pi^-\pi^+\pi^+$, have been used to identify the D mesons. The e^+p cross section for inclusive $D^{*\pm}$ production with $1 < Q^2 < 600\,\mathrm{GeV}^2$ and $0.02 < y < 0.7$ is $8.31 \pm 0.31(\mathrm{stat.})^{+0.30}_{-0.50}(\mathrm{syst.})$ nb in the kinematic region $1.5 < p_T(D^{*\pm}) < 15\,\mathrm{GeV}$ and $|\eta(D^{*\pm})| < 1.5$. Differential cross sections are consistent with a next-to-leading-order perturbative-QCD calculation when using charm-fragmentation models which take into account the interaction of the charm quark with the proton remnant. The observed cross section is extrapolated to the full kinematic region in $p_T(D^{*\pm})$ and $\eta(D^{*\pm})$ in order to determine the charm contribution, $F_2^{c\bar{c}}(x, Q^2)$, to the proton structure function. The ratio $F_2^{c\bar{c}}/F_2$ rises from $\simeq$10% at $Q^2 \simeq 1.8$ GeV^2 to $\simeq$30% at $Q^2 \simeq$130 GeV^2 for x values in the range 10^{-4} to 10^{-3}.

The ZEUS Collaboration

J. Breitweg, S. Chekanov, M. Derrick, D. Krakauer, S. Magill, B. Musgrave, A. Pellegrino, J. Repond, R. Stanek, R. Yoshida
Argonne National Laboratory, Argonne, IL, USA [p]

M.C.K. Mattingly
Andrews University, Berrien Springs, MI, USA

G. Abbiendi, F. Anselmo, P. Antonioli, G. Bari, M. Basile, L. Bellagamba, D. Boscherini[1], A. Bruni, G. Bruni, G. Cara Romeo, G. Castellini[2], L. Cifarelli[3], F. Cindolo, A. Contin, N. Coppola, M. Corradi, S. De Pasquale, P. Giusti, G. Iacobucci[4], G. Laurenti, G. Levi, A. Margotti, T. Massam, R. Nania, F. Palmonari, A. Pesci, A. Polini, G. Sartorelli, Y. Zamora Garcia[5], A. Zichichi
University and INFN Bologna, Bologna, Italy [f]

C. Amelung, A. Bornheim, I. Brock, K. Coböken, J. Crittenden, R. Deffner, M. Eckert[6], H. Hartmann, K. Heinloth, E. Hilger, H.-P. Jakob, A. Kappes, U.F. Katz, R. Kerger, E. Paul, J. Rautenberg[7],
H. Schnurbusch, A. Stifutkin, J. Tandler, A. Weber, H. Wieber
Physikalisches Institut der Universität Bonn, Bonn, Germany [c]

D.S. Bailey, O. Barret, W.N. Cottingham, B. Foster[8], G.P. Heath, H.F. Heath, J.D. McFall, D. Piccioni, J. Scott, R.J. Tapper
H.H. Wills Physics Laboratory, University of Bristol, Bristol, U.K. [o]

M. Capua, A. Mastroberardino, M. Schioppa, G. Susinno
Calabria University, Physics Dept.and INFN, Cosenza, Italy [f]

H.Y. Jeoung, J.Y. Kim, J.H. Lee, I.T. Lim, K.J. Ma, M.Y. Pac[9]
Chonnam National University, Kwangju, Korea [h]

A. Caldwell, W. Liu, X. Liu, B. Mellado, J.A. Parsons, S. Ritz[10], R. Sacchi, S. Sampson, F. Sciulli
Columbia University, Nevis Labs., Irvington on Hudson, N.Y., USA [q]

J. Chwastowski, A. Eskreys, J. Figiel, K. Klimek, K. Olkiewicz, M.B. Przybycień, P. Stopa, L. Zawiejski
Inst. of Nuclear Physics, Cracow, Poland [j]

L. Adamczyk[11], B. Bednarek, K. Jeleń, D. Kisielewska, A.M. Kowal, T. Kowalski, M. Przybycień, E. Rulikowska-Zarębska, L. Suszycki, J. Zając
Faculty of Physics and Nuclear Techniques, Academy of Mining and Metallurgy, Cracow, Poland [j]

Z. Duliński, A. Kotański
Jagellonian Univ., Dept. of Physics, Cracow, Poland [k]

L.A.T. Bauerdick, U. Behrens, J.K. Bienlein, C. Burgard, K. Desler, G. Drews, A. Fox-Murphy, U. Fricke, F. Goebel, P. Göttlicher, R. Graciani, T. Haas, W. Hain, G.F. Hartner, D. Hasell[12], K. Hebbel, K.F. Johnson[13], M. Kasemann[14], W. Koch, U. Kötz, H. Kowalski, L. Lindemann, B. Löhr, M. Martínez, J. Milewski[15], M. Milite, T. Monteiro[16], M. Moritz, D. Notz, F. Peluc-chi, M.C. Petrucci, K. Piotrzkowski, M. Rohde, P.R.B. Saull, A.A. Savin, U. Schneekloth, O. Schwarzer[17], F. Selonke, M. Sievers, S. Stonjek, E. Tassi, G. Wolf, U. Wollmer, C. Young-man, W. Zeuner
Deutsches Elektronen-Synchrotron DESY, Hamburg, Germany

B.D. Burow[18], C. Coldewey, H.J. Grabosch, A. Lopez-Duran Viani, A. Meyer, K. Mönig, S. Schlenstedt, P.B. Straub
DESY Zeuthen, Zeuthen, Germany

G. Barbagli, E. Gallo, P. Pelfer
University and INFN, Florence, Italy [f]

G. Maccarrone, L. Votano
INFN, Laboratori Nazionali di Frascati, Frascati, Italy [f]

A. Bamberger, S. Eisenhardt[19], P. Markun, H. Raach, S. Wölfle
Fakultät für Physik der Universität Freiburg i.Br., Freiburg i.Br., Germany [c]

N.H. Brook[20], P.J. Bussey, A.T. Doyle, S.W. Lee, N. Macdonald, G.J. McCance, D.H. Saxon, L.E. Sinclair, I.O. Skillicorn, E. Strickland, R. Waugh
Dept. of Physics and Astronomy, University of Glasgow, Glasgow, U.K. [o]

I. Bohnet, N. Gendner, U. Holm, A. Meyer-Larsen, H. Salehi, K. Wick
Hamburg University, I. Institute of Exp. Physics, Hamburg, Germany [c]

A. Garfagnini, I. Gialas[21], L.K. Gladilin[22], D. Kçira[23], R. Klanner, E. Lohrmann, G. Poelz, F. Zetsche
Hamburg University, II. Institute of Exp. Physics, Hamburg, Germany [c]

T.C. Bacon, J.E. Cole, G. Howell, L. Lamberti[24], K.R. Long, D.B. Miller, A. Prinias[25], J.K. Sedg-beer, D. Sideris, A.D. Tapper, R. Walker
Imperial College London, High Energy Nuclear Physics Group, London, U.K. [o]

U. Mallik, S.M. Wang
University of Iowa, Physics and Astronomy Dept., Iowa City, USA [p]

P. Cloth, D. Filges
Forschungszentrum Jülich, Institut für Kernphysik, Jülich, Germany

T. Ishii, M. Kuze, I. Suzuki[26], K. Tokushuku[27], S. Yamada, K. Yamauchi, Y. Yamazaki
Institute of Particle and Nuclear Studies, KEK, Tsukuba, Japan [g]

S.H. Ahn, S.H. An, S.J. Hong, S.B. Lee, S.W. Nam[28], S.K. Park
Korea University, Seoul, Korea [h]

H. Lim, I.H. Park, D. Son
Kyungpook National University, Taegu, Korea [h]

F. Barreiro, J.P. Fernández, G. García, C. Glasman[29], J.M. Hernández[30], L. Labarga, J. del Peso, J. Puga, I. Redondo[31], J. Terrón
Univer. Autónoma Madrid, Depto de Física Teórica, Madrid, Spain [n]

F. Corriveau, D.S. Hanna, J. Hartmann[32], W.N. Murray[33], A. Ochs, S. Padhi, M. Riveline, D.G. Stairs, M. St-Laurent, M. Wing
McGill University, Dept. of Physics, Montréal, Québec, Canada [a], [b]

T. Tsurugai
Meiji Gakuin University, Faculty of General Education, Yokohama, Japan

V. Bashkirov[34], B.A. Dolgoshein
Moscow Engineering Physics Institute, Moscow, Russia [l]

G.L. Bashindzhagyan, P.F. Ermolov, Yu.A. Golubkov, L.A. Khein, N.A. Korotkova, I.A. Korzhavina, V.A. Kuzmin, O.Yu. Lukina, A.S. Proskuryakov, L.M. Shcheglova[35], A.N. Solomin[35], S.A. Zotkin
Moscow State University, Institute of Nuclear Physics, Moscow, Russia [m]

C. Bokel, M. Botje, N. Brümmer, J. Engelen, E. Koffeman, P. Kooijman, A. van Sighem, H. Tiecke, N. Tuning, J.J. Velthuis, W. Verkerke, J. Vossebeld, L. Wiggers, E. de Wolf
NIKHEF and University of Amsterdam, Amsterdam, Netherlands [i]

D. Acosta[36], B. Bylsma, L.S. Durkin, J. Gilmore, C.M. Ginsburg, C.L. Kim, T.Y. Ling, P. Nylander
Ohio State University, Physics Department, Columbus, Ohio, USA [p]

H.E. Blaikley, S. Boogert, R.J. Cashmore[16], A.M. Cooper-Sarkar, R.C.E. Devenish, J.K. Edmonds, J. Große-Knetter[37], N. Harnew, T. Matsushita, V.A. Noyes[38], A. Quadt[16], O. Ruske, M.R. Sutton, R. Walczak, D.S. Waters
Department of Physics, University of Oxford, Oxford, U.K. [o]

A. Bertolin, R. Brugnera, R. Carlin, F. Dal Corso, S. Dondana, U. Dosselli, S. Dusini, S. Limentani, M. Morandin, M. Posocco, L. Stanco, R. Stroili, C. Voci
Dipartimento di Fisica dell' Università and INFN, Padova, Italy [f]

L. Iannotti[39], B.Y. Oh, J.R. Okrasiński, W.S. Toothacker, J.J. Whitmore
Pennsylvania State University, Dept. of Physics, University Park, PA, USA [q]

Y. Iga
Polytechnic University, Sagamihara, Japan [g]

G. D'Agostini, G. Marini, A. Nigro, M. Raso
Dipartimento di Fisica, Univ. 'La Sapienza' and INFN, Rome, Italy [f]

C. Cormack, J.C. Hart, N.A. McCubbin, T.P. Shah
Rutherford Appleton Laboratory, Chilton, Didcot, Oxon, U.K. [o]

D. Epperson, C. Heusch, H.F.-W. Sadrozinski, A. Seiden, R. Wichmann, D.C. Williams
University of California, Santa Cruz, CA, USA [p]

N. Pavel
Fachbereich Physik der Universität-Gesamthochschule Siegen, Germany [c]

H. Abramowicz[40], S. Dagan[41], S. Kananov[41], A. Kreisel, A. Levy[41]
Raymond and Beverly Sackler Faculty of Exact Sciences, School of Physics, Tel-Aviv University, Tel-Aviv, Israel [e]

T. Abe, T. Fusayasu, M. Inuzuka, K. Nagano, K. Umemori, T. Yamashita
Department of Physics, University of Tokyo, Tokyo, Japan [g]

R. Hamatsu, T. Hirose, K. Homma[42], S. Kitamura[43], T. Nishimura
Tokyo Metropolitan University, Dept. of Physics, Tokyo, Japan [g]

M. Arneodo[44], N. Cartiglia, R. Cirio, M. Costa, M.I. Ferrero, S. Maselli, V. Monaco, C. Peroni, M. Ruspa, A. Solano, A. Staiano
Università di Torino, Dipartimento di Fisica Sperimentale and INFN, Torino, Italy [f]

M. Dardo
II Faculty of Sciences, Torino University and INFN - Alessandria, Italy [f]

D.C. Bailey, C.-P. Fagerstroem, R. Galea, T. Koop, G.M. Levman, J.F. Martin, R.S. Orr, S. Polenz, A. Sabetfakhri, D. Simmons
University of Toronto, Dept. of Physics, Toronto, Ont., Canada [a]

J.M. Butterworth, C.D. Catterall, M.E. Hayes, E.A. Heaphy, T.W. Jones, J.B. Lane, B.J. West
University College London, Physics and Astronomy Dept., London, U.K. [o]

J. Ciborowski, R. Ciesielski, G. Grzelak, R.J. Nowak, J.M. Pawlak, R. Pawlak, B. Smalska, T. Tymieniecka, A.K. Wróblewski, J.A. Zakrzewski, A.F. Żarnecki
Warsaw University, Institute of Experimental Physics, Warsaw, Poland [j]

M. Adamus, T. Gadaj
Institute for Nuclear Studies, Warsaw, Poland [j]

O. Deppe, Y. Eisenberg[41], D. Hochman, U. Karshon[41]
Weizmann Institute, Department of Particle Physics, Rehovot, Israel [d]

W.F. Badgett, D. Chapin, R. Cross, C. Foudas, S. Mattingly, D.D. Reeder, W.H. Smith, A. Vaiciulis[45], T. Wildschek, M. Wodarczyk
University of Wisconsin, Dept. of Physics, Madison, WI, USA [p]

A. Deshpande, S. Dhawan, V.W. Hughes
Yale University, Department of Physics, New Haven, CT, USA [p]

S. Bhadra, W.R. Frisken, R. Hall-Wilton, M. Khakzad, S. Menary, W.B. Schmidke
York University, Dept. of Physics, Toronto, Ont., Canada [a]

[1] now visiting scientist at DESY
[2] also at IROE Florence, Italy
[3] now at Univ. of Salerno and INFN Napoli, Italy
[4] also at DESY
[5] supported by Worldlab, Lausanne, Switzerland
[6] now at BSG Systemplanung AG, 53757 St. Augustin
[7] drafted to the German military service
[8] also at University of Hamburg, Alexander von Humboldt Research Award
[9] now at Dongshin University, Naju, Korea
[10] now at NASA Goddard Space Flight Center, Greenbelt, MD 20771, USA
[11] supported by the Polish State Committee for Scientific Research, grant No. 2P03B14912
[12] now at Massachusetts Institute of Technology, Cambridge, MA, USA
[13] visitor from Florida State University
[14] now at Fermilab, Batavia, IL, USA
[15] now at ATM, Warsaw, Poland
[16] now at CERN
[17] now at ESG, Munich
[18] now an independent researcher in computing
[19] now at University of Edinburgh, Edinburgh, U.K.
[20] PPARC Advanced fellow
[21] visitor of Univ. of Crete, Greece, partially supported by DAAD, Bonn - Kz. A/98/16764
[22] on leave from MSU, supported by the GIF, contract I-0444-176.07/95
[23] supported by DAAD, Bonn - Kz. A/98/12712
[24] supported by an EC fellowship
[25] PPARC Post-doctoral fellow
[26] now at Osaka Univ., Osaka, Japan
[27] also at University of Tokyo
[28] now at Wayne State University, Detroit
[29] supported by an EC fellowship number ERBFMBICT 972523
[30] now at HERA-B/DESY supported by an EC fellowship No.ERBFMBICT 982981
[31] supported by the Comunidad Autonoma de Madrid
[32] now at debis Systemhaus, Bonn, Germany
[33] now a self-employed consultant
[34] now at Loma Linda University, Loma Linda, CA, USA
[35] partially supported by the Foundation for German-Russian Collaboration DFG-RFBR (grant no. 436 RUS 113/248/3 and no. 436 RUS 113/248/2)
[36] now at University of Florida, Gainesville, FL, USA
[37] supported by the Feodor Lynen Program of the Alexander von Humboldt foundation
[38] now with Physics World, Dirac House, Bristol, U.K.
[39] partly supported by Tel Aviv University
[40] an Alexander von Humboldt Fellow at University of Hamburg
[41] supported by a MINERVA Fellowship
[42] now at ICEPP, Univ. of Tokyo, Tokyo, Japan
[43] present address: Tokyo Metropolitan University of Health Sciences, Tokyo 116-8551, Japan
[44] now also at Università del Piemonte Orientale, I-28100 Novara, Italy, and Alexander von Humboldt fellow at the University of Hamburg
[45] now at University of Rochester, Rochester, NY, USA

[a] supported by the Natural Sciences and Engineering Research Council of Canada (NSERC)
[b] supported by the FCAR of Québec, Canada
[c] supported by the German Federal Ministry for Education and Science, Research and Technology (BMBF), under contract numbers 057BN19P, 057FR19P, 057HH19P, 057HH29P, 057SI75I
[d] supported by the MINERVA Gesellschaft für Forschung GmbH, the German Israeli Foundation, and by the Israel Ministry of Science
[e] supported by the German-Israeli Foundation, the Israel Science Foundation, the U.S.-Israel Binational Science Foundation, and by the Israel Ministry of Science
[f] supported by the Italian National Institute for Nuclear Physics (INFN)
[g] supported by the Japanese Ministry of Education, Science and Culture (the Monbusho) and its grants for Scientific Research
[h] supported by the Korean Ministry of Education and Korea Science and Engineering Foundation
[i] supported by the Netherlands Foundation for Research on Matter (FOM)
[j] supported by the Polish State Committee for Scientific Research, grant No. 115/E-343/SPUB/P03/154/98, 2P03B03216, 2P03B04616, 2P03B10412, 2P03B03517, and by the German Federal Ministry of Education and Science, Research and Technology (BMBF)
[k] supported by the Polish State Committee for Scientific Research (grant No. 2P03B08614 and 2P03B06116)
[l] partially supported by the German Federal Ministry for Education and Science, Research and Technology (BMBF)
[m] supported by the Fund for Fundamental Research of Russian Ministry for Science and Education and by the German Federal Ministry for Education and Science, Research and Technology (BMBF)
[n] supported by the Spanish Ministry of Education and Science through funds provided by CICYT
[o] supported by the Particle Physics and Astronomy Research Council
[p] supported by the US Department of Energy
[q] supported by the US National Science Foundation

1 Introduction

The first HERA measurements of the charm contribution, $F_2^{c\bar{c}}$, to the proton structure function F_2 were reported by the H1 and ZEUS collaborations from the analyses of their 1994 deep inelastic scattering (DIS) data sets [1, 2]. These early results, which were statistically limited, revealed a steep rise of $F_2^{c\bar{c}}$ as Bjorken-x decreases. At the lowest accessible x values, it was found that around 25% of DIS events contained open charm, in contrast to the EMC fixed target measurements [3] in the high-x region where the charm contribution is small. Given the large charm content, the correct theoretical treatment of charm for F_2 analyses in the HERA regime has become essential. More detailed measurements of charm production will aid such analyses.

The early results [1, 2] suggested that the production dynamics of charmed mesons in ep collisions are dominated by the boson-gluon-fusion (BGF) mechanism shown in Fig. 1. In this case, the reactions $e^+p \to e^+D^{*\pm}X$ are sensitive to the gluon distribution in the proton [4]. The measurement of charm production can also provide tests of perturbative QCD (pQCD), in particular, tests of the hard scattering factorization theorem, which states that the same, universal, gluon distribution should contribute to both F_2 and $F_2^{c\bar{c}}$. In addition, the presence of two large scales, namely, the virtuality of the exchanged boson (Q^2) and the square of the charm-quark mass (m_c^2), provides a testing ground for resummation techniques.

This paper reports a measurement of $D^{*\pm}(2010)$ production using the 1996 and 1997 data sets collected with the ZEUS detector, corresponding to an integrated luminosity of 37 pb^{-1}. During this period, HERA collided $E_e = 27.5$ GeV positrons with $E_p = 820$ GeV protons, yielding a center-of-mass energy, $\sqrt{s}$, of 300 GeV. This larger data sample, together with some improvements to the ZEUS detector, allows an extension of the kinematic range to both larger and smaller Q^2. The $D^{*\pm}$ production is investigated in the decay channel $D^{*+}(2010) \to D^0(1864)\pi_s^+$ (+ c.c.), where π_s^+ refers to a slow π^+ [5], followed by the D^0 decay channels $D^0 \to K^-\pi^+$ (+ c.c.) or $D^0 \to K^-\pi^+\pi^-\pi^+$ (+ c.c.). These two final states will be referred to as the $K2\pi$ and $K4\pi$ channels, respectively.

Following a brief discussion of three pQCD calculations for $D^{*\pm}$ production in DIS, a description of the experiment and details of the data analysis are provided. Next, the cross sections for $D^{*\pm}$ are presented and are compared to the QCD predictions. A possible cause of the observed discrepancies between the data and the QCD results is discussed. Finally, the $D^{*\pm}$ results are used to obtain the charm contribution to F_2.

2 Charm quark production models

General agreement was found between the earlier HERA $D^{*\pm}$ data and the results from a Monte Carlo program HVQDIS [6] for the production of heavy quarks and their subsequent fragmentation to hadrons. This program is based on next-to-leading-order (NLO) calculations [7] of order α_s^2 in the coefficient functions in the so-called fixed-flavor-number scheme (FFNS). In this scheme, the number of active quark flavors is fixed, independent of Q^2. Only light quarks ($u,\ d,\ s$) are included in the initial-state proton and charm quarks are produced exclusively by BGF with NLO processes [8]. The presence of the two large scales, Q^2 and m_c^2, can spoil the convergence of the perturbative series because the neglected terms of orders higher than α_s^2 contain $\log(Q^2/m_c^2)$ factors that can become large. Therefore the results of HVQDIS are expected to be most accurate at $Q^2 \approx m_c^2$ and to become less reliable when $Q^2 \gg m_c^2$.

In this high Q^2 region, the c quark can be treated as massless, as implemented in the zero-

mass, variable-flavor-number scheme (ZM-VFNS). In this scheme, the resummation of large logarithms of Q^2/m_c^2 [9, 10] results in a charm density which is added as a fourth flavor and which is then evolved in the same way as the light quark densities. At intermediate Q^2 values, the two schemes need to be merged. One way in which this is done is described by ACOT [9] and by Collins [11]. An alternative matching method has been proposed by MRST [12].

A third method for modelling $D^{*\pm}$ production has recently been suggested by BKL [13]. This tree-level pQCD calculation, applicable for $p_T \geq m_c$, considers the hadronization of the $(c\bar{q})$-state into a D^*, in contrast to hadronizing an isolated c-quark. The D^* is created from both color singlet and color octet configurations of the light and heavy quarks. Results from e^+e^- annihilation imply that the octet contribution is small. However, the singlet contribution alone underestimates [13] the ZEUS data on the photoproduction of charm [14]. This calculation has been extended to DIS charm production and is compared to the $D^{*\pm}$ data reported here.

3 Experimental setup

ZEUS is a multipurpose detector which has been described in detail elsewhere [15]. The key component for this analysis is the central tracking detector (CTD) which operates in a magnetic field of 1.43 T provided by a thin superconducting solenoid. The CTD [16] is a drift chamber consisting of 72 cylindrical layers, arranged in 9 superlayers covering the polar angle[1] region $15^\circ < \theta < 164^\circ$. The transverse momentum resolution for full-length tracks is $\sigma(p_{\rm T})/p_{\rm T} = 0.0058\, p_{\rm T} \oplus 0.0065 \oplus 0.0014/p_{\rm T}$ ($p_{\rm T}$ in GeV). The CTD was also used to establish an interaction vertex for each event.

The uranium-scintillator sampling calorimeter (CAL) surrounds the solenoid. The CAL is hermetic and consists of 5918 cells, each read out by two photomultiplier tubes. The CAL contains three parts, the forward (FCAL), barrel (BCAL) and rear (RCAL), with longitudinal segmentation into electromagnetic and hadronic sections. The energy resolutions, as measured in test beams, are $\sigma/E = 0.18/\sqrt{E(\text{GeV})}$ and $0.35/\sqrt{E(\text{GeV})}$ for electrons and hadrons, respectively [17].

The position of positrons scattered close to the positron beam direction is determined by a scintillator strip detector (SRTD) [18]. The luminosity was measured from the rate of the bremsstrahlung process, $e^+p \to e^+\gamma p$, where the photon is measured by a lead/scintillator calorimeter [19] located at $Z = -107\,\text{m}$ in the HERA tunnel.

4 Kinematics and reconstruction of variables

The reaction $e^+(k) + p(P) \to e^+(k') + X$ at fixed squared center-of-mass energy, $s = (k+P)^2$, is described in terms of $Q^2 = -q^2 = -(k-k')^2$ and Bjorken-$x = Q^2/(2P\cdot q)$. The fractional energy transferred to the proton in its rest frame is $y = Q^2/(sx)$. The virtual photon (γ^*)-proton center-of-mass energy W, given by $W^2 = (q+P)^2$, is also used, see Fig. 1.

In neutral current (NC) e^+p DIS, both the final-state positron, with energy E'_e and angle θ'_e, and the hadronic system (with a characteristic angle γ_h, which, in the simple quark-parton model, is the polar angle of the struck quark) can be measured. The scattered positron was identified using an algorithm based on a neural network [20]. CAL cells were combined to form

[1] The ZEUS coordinate system is defined as right-handed with the Z axis pointing in the forward (proton beam) direction and the X axis horizontal pointing towards the center of HERA. The origin is at the nominal ep interaction point. The polar angle θ is defined with respect to the positive Z direction.

clusters and combinations of these clusters and CTD tracks were used to reconstruct energy-flow objects (EFO's) [21, 22]. For perfect detector resolution and acceptance, the quantity $\delta \equiv \Sigma_i(E_i - p_{z,i})$ is equal to $2E_e$ (55 GeV). Here, E_i and $p_{z,i}$ are the energy and longitudinal component of the momentum assigned to the i-th EFO. The sum runs over all EFO's including those assigned to the scattered positron.

In the $K2\pi$ analysis, Q^2 was reconstructed from the scattered positron (Q^2_e) with the electron method [23] and y with the so-called Σ method [24]

$$y_\Sigma = \frac{\delta_{had}}{\delta}, \tag{1}$$

where δ_{had} is calculated in the same way as δ but excluding the EFO's assigned to the scattered positron. Bjorken-x ($x_{e\Sigma}$) and W ($W_{e\Sigma}$) are then defined by a combination of Q^2_e and y_Σ ($e\Sigma$ method).

The fractional momentum of the $D^{*\pm}$ in the $\gamma^* p$ system is defined as

$$x(D^*) = \frac{2|\vec{p}^{\,*}(D^*)|}{W}, \tag{2}$$

where $\vec{p}^{\,*}(D^*)$ is the $D^{*\pm}$ momentum in the $\gamma^* p$ center-of-mass frame. For the boost to the $\gamma^* p$ system, the virtual-photon vector was reconstructed using the double-angle (DA) estimator [23] of the scattered positron energy, E'_{DA}. In this method, only the angles θ'_e and γ_h are used [25]. E'_{DA} is less sensitive to radiative effects at the leptonic vertex than the scattered e^+ energy determined using the electron method.

For the $K4\pi$ analysis, Q^2, x and W were determined using the DA estimators (Q^2_{DA}, x_{DA} and W_{DA}).

5 Monte Carlo simulation

A GEANT 3.13-based [26] Monte Carlo (MC) simulation program which incorporates the best current knowledge of the ZEUS detector and trigger was used to correct the data for detector and acceptance effects. The event generator used for the simulation of the QED radiation from the leptonic vertex was RAPGAP [27] interfaced to HERACLES 4.1 [28]. The charm quarks were produced in the BGF process calculated at leading order (LO). The charm mass was set to 1.5 GeV. The GRV94HO [29] parton distribution functions (pdf's) were used for the proton. Fragmentation was carried out using the Lund model [30], as implemented in JETSET 7.4 [31], with the full parton shower option. The fraction of the original c-quark momentum which is carried by the $D^{*\pm}$ is determined from the 'SLAC' fragmentation function, which is equivalent to the Peterson model [32], with the fragmentation parameter ϵ set to 0.035 [33]. The HERWIG 5.9 [34] event generator was also used, with the same pdf's and c-quark mass as used in RAPGAP, to investigate the effects of fragmentation.

Generated events with at least one $D^{*+} \to D^0\pi^+_s \to (K^-\pi^+$ or $K^-\pi^+\pi^-\pi^+)\pi^+_s$ (or c.c.) were selected. These events were then processed through the detector and trigger simulation and through the same reconstruction program as was used for the data.

6 Event selection

6.1 Trigger

Events were selected online with a three-level trigger [15]. At the first level (FLT), inclusive DIS events are triggered by the presence of an isolated electromagnetic cluster in the RCAL or any energy deposition in excess of 3 GeV in any electromagnetic section of the CAL [35]. During high-luminosity periods, when the rate was high, a coincidence with an FLT track was also required. Tracks at the FLT are defined as a series of CTD hits pointing to the nominal interaction point. The efficiency of this trigger, with respect to the calorimeter-only trigger, was greater than 99.5% and in good agreement with the MC simulation.

At the second level, algorithms are applied to reduce the non-e^+p background. The full event information is available at the third level trigger (TLT). At this level, events are accepted as DIS candidates if a high-energy scattered positron candidate is found within the CAL ('inclusive DIS trigger'). Because of the high rate of low-Q^2 events, this trigger was turned off in the region around the RCAL beampipe during high-luminosity operation. For the $K2\pi$ decay channel, a D^*-finder (based on computing the $K\pi\pi$ mass using tracking information and selecting loosely around the $D^{*\pm}$ mass) was available in the TLT. Events at low Q^2 were then kept by requiring a coincidence of an identified scattered positron anywhere in the CAL and a tagged $D^{*\pm}$ candidate. This will be referred to as the 'D^* trigger'.

Using data selected from periods when both triggers were in use, the relative efficiency of the D^* trigger with respect to the inclusive DIS trigger is found to be about 80% and independent of Q^2, x, $p_T(D^*)$ and $\eta(D^*)$ within the measured kinematic regions. The MC simulations reproduce this efficiency to an accuracy better than the statistical accuracy of the data ($\approx$ 2%).

6.2 Offline selection

The DIS event selection was similar to that described in an earlier publication [36]; namely, the selection required:

- a positron, as identified by a neural network algorithm, with a corrected energy above 10 GeV;
- the impact point of the scattered positron on the RCAL was required to lie outside the region 26×14 cm^2 centered on the RCAL beamline;
- $40 < \delta < 65$ GeV; and
- a Z-vertex position $|Z_{vtx}| < 50$ cm.

The DIS events were restricted to the kinematic region

- $1 < Q^2 < 600$ GeV^2 and $0.02 < y < 0.7$.

$D^{*\pm}$ candidates were reconstructed from CTD tracks which were assigned to the reconstructed event vertex. Only tracks with at least one hit in the third superlayer of the CTD were considered. This corresponds to an implicit requirement that $p_T > 0.075$ GeV. Tracks were also required to have $|\eta| < 1.75$, where the pseudorapidity is defined as $\eta = -\ln(\tan\frac{\theta}{2})$. The selected tracks were in the region where the CTD performance is well understood. For these tracks the reconstruction efficiency is above 95%.

$D^{*\pm}$ production was measured in the decay channel $D^{*+} \to D^0\pi_s^+$ (+ c.c.), which has a branching ratio of 0.683 ± 0.014 [37], followed by the D^0 decays $D^0 \to K^-\pi^+$ (+ c.c.) or $D^0 \to K^-\pi^+\pi^-\pi^+$ (+ c.c.). The branching ratio for D^0 to $K\pi$ ($K3\pi$) is 0.0385 ± 0.0009 (0.076 ± 0.004) [37]. The remaining selection criteria were different for the two final states and are discussed separately.

6.3 Selection for the $K2\pi$ final state

Pairs of oppositely-charged tracks were first combined to form a D^0 candidate. Since no particle identification was performed, the tracks were alternatively assigned the masses of a charged kaon and a charged pion. An additional slow track, with charge opposite to that of the kaon track and assigned the pion mass (π_s), was combined with the D^0 candidate to form a $D^{*\pm}$ candidate.

The combinatorial background for the $K2\pi$ decay channel was further reduced by requiring

- that the transverse momenta of the K and the π were greater than 0.4 GeV, and that of the π_s was greater than 0.12 GeV.

In addition, the momentum ratio requirement

- $p(D^0)/p(\pi_s) > 8.0$

was imposed. This requirement was used in the D^* trigger to reduce the rate of candidate events with large $\Delta M \equiv (M_{K\pi\pi_s} - M_{K\pi})$, far from the signal region.

The $D^{*\pm}$ kinematic region of the present analysis was defined as

- $1.5 < p_T(D^*) < 15$ GeV and $|\eta(D^*)| < 1.5$.

Finally, the signal regions for the mass of the D^0 candidate, $M(D^0)$, and ΔM were

- $1.80 < M(D^0) < 1.92$ GeV, and
- $143 < \Delta M < 148$ MeV.

6.4 Selection for the $K4\pi$ final state

Permutations of two negatively- and two positively-charged tracks were first combined to form a D^0 candidate. As for the $K2\pi$ channel, the tracks were alternatively assigned the masses of a charged kaon and a charged pion. An additional track, with charge opposite to that of the kaon track and assigned the pion mass (π_s), was combined with the D^0 candidate to form a $D^{*\pm}$ candidate. The combinatorial background for the $K4\pi$ decay channel was reduced by requiring

- that the transverse momentum of the K and each π was greater than 0.5 and 0.2 GeV, respectively, and that of the π_s was greater than 0.15 GeV.

In addition, the momentum ratio requirement

- $p(D^0)/p(\pi_s) > 9.5$

was imposed.

The $D^{*\pm}$ kinematic region was defined as

- $2.5 < p_T(D^*) < 15$ GeV and $|\eta(D^*)| < 1.5$.

The signal regions for $M(D^0)$ and $\Delta M \equiv (M_{K\pi\pi\pi\pi_s} - M_{K\pi\pi\pi})$ were

- $1.81 < M(D^0) < 1.91$ GeV, and
- $143 < \Delta M < 148$ MeV.

6.5 Mass distributions

Figures 2(a) and (c) show the distributions of $M(D^0)$ for candidates with ΔM in the signal region for the two final states, while Figs. 2(b) and (d) show the distributions of ΔM for candidates with $M(D^0)$ in the signal region. Clear signals are observed around the expected mass values.

For the $K2\pi$ final state, a fit to the $M(D^0)$ distribution of two Gaussians plus an exponentially falling background gives a peak at $M(D^0) = 1863.2 \pm 0.8$ MeV and a width of 23 ± 2 MeV. The second Gaussian around 1.6 GeV in Fig. 2(a) originates primarily from D^0 decays to $K^-\pi^+\pi^0$ in which the neutral pion is not reconstructed. For the $K4\pi$ channel, the background level was determined by using the side-bands outside the ΔM signal region (see the dashed histogram in Fig. 2(c)) to make a $M(D^0)$ distribution. The fit to the $M(D^0)$ distribution, made by adding a Gaussian to the background distribution, yielded $M(D^0) = 1862.7 \pm 1.5$ MeV and a width of 20 ± 2 MeV. The deviations of the data from the fit, visible in the region just above the signal in Fig. 2(c), are mostly due to the mass misassignments of the K and π candidates with the same charge from D^0 decay. This was verified by MC studies [38]. The mass values found for the D^0 are consistent with the PDG [37] value of 1864.6 ± 0.5 MeV.

The solid curve in Fig. 2(b) shows a binned maximum-likelihood fit to the ΔM distribution from the $K2\pi$ channel using a Gaussian plus a background of the form $A(\Delta M - m_\pi)^B \exp[C(\Delta M - m_\pi)]$, where A, B and C are free parameters and m_π is the pion mass. The fit to the $K2\pi$ plot gives a peak at $\Delta M = 145.44 \pm 0.05$ MeV, in good agreement with the PDG value of 145.397 ± 0.030 MeV, and a width of 0.79 ± 0.05 MeV, in agreement with the experimental resolution. The multiplicative exponential term is needed to describe the background suppression at large ΔM, which comes from the requirement on the momentum ratio $p(D^0)/p(\pi_s)$.

The solid curve in Fig. 2(d) shows a fit of the ΔM distribution from the $K4\pi$ channel using a Gaussian plus a background distribution obtained from the side-bands outside the $M(D^0)$ signal region (see the dashed histogram in Fig. 2(d)). The fit yields a peak at $\Delta M = 145.61 \pm 0.05$ MeV and a width of 0.78 ± 0.07 MeV.

For the $K2\pi$ channel, the number of $D^{*\pm}$ events obtained from a fit to the ΔM distribution in the restricted region of Q^2, y, $p_T(D^*)$ and $\eta(D^*)$ is 2064 ± 72. The number of events in the $K4\pi$ channel is determined from the ΔM distribution using the side band method [14], which properly accounts for the combinatorial background and the background arising from the mass misassignments. The side bands, $1.74 < M(K\pi\pi\pi) < 1.79$ GeV and $1.93 < M(K\pi\pi\pi) < 1.98$ GeV, were normalized to the ΔM distribution in the region $150 < \Delta M < 160$ MeV. The number of $D^{*\pm}$ events in the $K4\pi$ channel is found to be 1277 ± 124 in the restricted kinematic region of the measurement.

7 Data characteristics

The properties of the selected events are compared with those of the RAPGAP Monte Carlo simulation. All distributions shown are background-subtracted since they represent the number of signal events obtained by fitting the various mass distributions in a given bin. The data for the $K2\pi$ channel are shown in Figs. 3 and 4 as solid points and the RAPGAP simulation as shaded histograms. All MC plots are normalized to have the same area as the data distributions.

Figure 3 shows histograms of E'_e, θ'_e, γ_h and δ and Fig. 4(a-c) displays the distributions of Q^2_e, $x_{e\Sigma}$ and $W_{e\Sigma}$. In general, reasonable agreement is observed between data and the MC simulation. Figure 4(d-f) shows the transverse momentum, $p_T(D^*)$, the pseudorapidity, $\eta(D^*)$, and the energy fraction carried by the $D^{*\pm}$ in the $\gamma^* p$ center-of-mass frame, $x(D^*)$. Although the $p_T(D^*)$ spectrum of the data is well described, the MC pseudorapidity spectrum is shifted to lower η compared to the data and the $x(D^*)$ spectrum for the MC is shifted to slightly larger values. These discrepancies are examined in more detail below.

The HERWIG [34] Monte Carlo was used for systematic studies. This MC describes the $D^{*\pm}$ differential distributions better than RAPGAP, but does not give as good agreement with the DIS variables as RAPGAP since it does not contain QED radiative effects.

Photoproduction, where the final positron is scattered through very small angles and escapes undetected through the RCAL beamhole, is a possible background source. Hadronic activity in the RCAL can be wrongly identified as the scattered positron, giving rise to fake DIS events. The effect was investigated using a large sample of photoproduced $D^{*\pm}$ events generated with the HERWIG MC. After the final selection cuts the photoproduction contamination is found to be less than 1%, much smaller than the statistical error of the measurement, and so is neglected.

The overall contribution to $D^{*\pm}$ production from b quark decays in the measured kinematic region is estimated to be less than 2%, using HVQDIS with $m_b = 4.5$ GeV and a hadronization fraction of $b \to D^*$ of 0.173 [39]. A similar study using RAPGAP yields an estimate of $\sim$1% at low Q^2 and less than 3% at high Q^2. Hence the contribution from b quark decays has been neglected.

8 Systematic uncertainties

The experimental systematic uncertainties in the cross section are grouped into several major categories:

- Systematic uncertainties related to the inclusive DIS selection of the events: variations were made in the y cut, the RCAL box cut, and the vertex position cut. In addition, for the $K2\pi$ final state both Q^2 and y were determined using the DA method rather than using the $e\Sigma$ method. The combined variations resulted in a change of $\pm 1.5\%$ to the nominal cross section. For the $K4\pi$ channel, the electron method was used rather than the DA method and the combined variations resulted in a change of $\pm 4.7\%$.

- Systematic uncertainties in the $D^{*\pm}$ selection: for the $K2\pi$ final state, the minimum transverse momentum of tracks used in the $D^{*\pm}$ reconstruction was raised and lowered by up to 100 MeV for the K and π and by 25 MeV for the π_s and resulted in a $\pm 4.5\%$ variation. The momentum ratio $p(D^0)/p(\pi_s)$ was raised by $+0.5$ and yielded a negligible change. For the $K4\pi$ channel, similar changes in the minimum transverse momenta and varying $p(D^0)/p(\pi_s)$ by ± 0.5 combine to give a $\pm 8.5\%$ variation.

- Systematic uncertainties related to the estimation of the number of events and background uncertainty: for the $K2\pi$ analysis, a χ^2 ΔM-fit instead of a (binned) logarithmic-likelihood fit was performed. The $M(D^0)$ signal range, within which the ΔM distributions were fitted, was varied by ± 10 MeV. These variations resulted in a change of $\pm 2.5\%$. For the $K4\pi$ analysis, the $M(D^0)$ signal range was also varied by ± 10 MeV and the width of the side-bands used to estimate combinatorial background was varied. These variations resulted in a change of $\pm 5.8\%$.

- The systematic uncertainty related to the MC generator was estimated for the $K2\pi$ analysis by using the HERWIG MC generator to calculate the corrections for the cross section determination. This variation yields a change of -1.3%. The larger overall systematic uncertainty for the $K4\pi$ channel means that this systematic uncertainty was negligible for this channel.

- Since approximately 10% of the $D^{*\pm}$ events [40] are produced through a diffractive mechanism which was not included in the Monte Carlo generators used to correct the data, acceptance corrections have also been obtained using a sample of diffractive events generated with RAPGAP. The difference in the global correction factor for the diffractive events was less than 10%. This yielded a 1.3% variation in the overall cross section and was neglected.

- The systematic uncertainty related to the trigger for the $K2\pi$ final state was estimated to be $\pm 1\%$ by an analysis using only the inclusive DIS triggers and was neglected.

- The overall normalization uncertainties due to the luminosity measurement error of $\pm 1.65\%$, and those due to the $D^{*\pm}$ and D^0 decay branching ratios [37] were not included in the systematic uncertainties.

The systematic uncertainties were added in quadrature. The total systematic uncertainty is less than the statistical error for most of the differential distributions and is of the same order as the statistical error for the integrated cross section.

9 Cross sections

The cross sections for a given observable Y were determined from the equation:

$$\frac{d\sigma}{dY} = \frac{N}{A \cdot \mathcal{L} \cdot B \cdot \Delta Y} \tag{3}$$

where N is the number of $D^{*\pm}$ events in a bin of ΔY, A is the acceptance (including migrations, efficiencies and radiative effects) for that bin, $\mathcal{L}$ is the integrated luminosity and B is the product of the appropriate branching ratios for the $D^{*\pm}$ and D^0.

The RAPGAP MC was used to estimate the acceptance. In the $K2\pi$ ($K4\pi$) kinematic region the overall acceptance was 25.4 (18.0)%. The statistical error of the MC is negligible compared to that of the data.

The measured cross section in the region $1 < Q^2 < 600$ GeV^2, $0.02 < y < 0.7$, for $1.5 < p_T(D^*) < 15$ GeV and $|\eta(D^*)| < 1.5$ using the $K2\pi$ final state, is

$$\sigma(e^+p \to e^+D^{*\pm}X) = 8.31 \pm 0.31(\text{stat.})^{+0.30}_{-0.50}(\text{syst.}) \text{ nb},$$

and for $2.5 < p_T(D^*) < 15$ GeV and $|\eta(D^*)| < 1.5$ the cross section using the $K4\pi$ channel is

$$\sigma(e^+p \to e^+D^{*\pm}X) = 3.65 \pm 0.36(\text{stat.})^{+0.20}_{-0.41}(\text{syst.}) \text{ nb.}$$

These results are in good agreement with the HVQDIS [6] calculations of 8.44 and 4.13 nb, respectively. The parton distribution functions resulting from a ZEUS NLO QCD fit [41] to the ZEUS, NMC and BCDMS data were used in these calculations. In this fit, only the gluon and three light quark flavors were assumed to be present. HVQDIS fragments the charm quark to a $D^{*\pm}$ using the Peterson fragmentation function. For the above calculation, m_c was set to 1.4 GeV, the Peterson fragmentation parameter ϵ=0.035, and the mass factorization and renormalization scales were both set to $\sqrt{4m_c^2 + Q^2}$. The hadronization fraction $f(c \to D^{*+})$ was set to $0.222 \pm 0.014 \pm 0.014$, as measured by the OPAL collaboration [39]. The result is, however, sensitive to the choice of the parameters. For example, varying m_c from 1.3 to 1.5 GeV results in a variation of $\pm$0.55 nb to the $K2\pi$ prediction of 8.44 nb. If, instead of using the ZEUS NLO parton distributions, the three-flavor GRV98HO [42] set is used, the calculated cross section for the $K2\pi$ kinematic region, assuming a charm mass of 1.4 GeV, is reduced from 8.44 nb to 7.00 nb.

Figures 5 and 6 show the $D^{*\pm}$ differential cross sections in the measured kinematic regions. The data points are drawn at the bin center of gravity, which is defined as the point at which the value of the assumed theoretical curve (HVQDIS with central choice of parameters and RAPGAP fragmentation, see the discussion below) equals the mean value of the curve in the bin. The cross sections are compiled in Table 1. The 9% error on $f(c \to D^{*+})$ introduces an extra normalization uncertainty on the theoretical predictions which is not shown.

The data are compared with two different theoretical calculations. There is good agreement with HVQDIS, shown as the open bands in Fig. 5, except for the $\eta(D^*)$ and $x(D^*)$ distributions, where the HVQDIS calculations show a shift with respect to the data to more negative $\eta(D^*)$ values and larger $x(D^*)$ values.

The disagreement between the $\eta(D^*)$ distribution and HVQDIS has also been observed by the H1 collaboration in their DIS charm production data [4]. A large discrepancy in the $\eta(D^*)$ distribution is also observed [14] between the ZEUS photoproduction of charm and a massive NLO calculation [43]. The discrepancy in shapes between the data and the HVQDIS prediction could result from the use of the Peterson fragmentation function. This predicts the magnitude of the momentum of the D^{*+} from $c \to D^{*+}$ but produces no D^{*+} transverse momentum relative to the c quark. In addition, no QCD evolution is included. In contrast, the fragmentation models in JETSET and HERWIG predict a migration of the charm quark emerging from the hard interaction towards positive pseudorapidities as it fragments into a D^{*+} due to the interaction between the color charges of the c quark and the proton remnant. This has been called the 'beam-drag effect' [44].

To quantify the contribution of these fragmentation effects to the predicted $D^{*\pm}$ differential cross sections, the RAPGAP Monte Carlo charm quark distribution was reweighted to match the two dimensional $p_T(c)$, $\eta(c)$ distributions for the charm quarks from HVQDIS. The fragmentation of these quarks was simulated by the Monte Carlo program including parton shower effects[2]. This reweighting procedure leads to an improved description of the data, as can be seen in Fig. 5 (shaded bands), where the two different implementations of the $c \to D^{*+}$ fragmentation are compared. In order to study systematic effects, the same procedure as above was

[2]Note that this procedure keeps the cross section in the overall phase space in $p_T(D^*)$ and $\eta(D^*)$ equal to the HVQDIS result and is equivalent to applying the RAPGAP fragmentation to the HVQDIS charm quark prediction.

followed but with the parton shower option switched off and HERWIG used. This produced qualitatively similar results to the nominal method[3]. The data are again compared to the HVQDIS calculation including the RAPGAP-based fragmentation in Fig. 6. The solid curves are from using $m_c = 1.4$ GeV, corresponding to the central mass value of the shaded band in Fig. 5.

The data are also compared in Fig. 6 with the BKL tree-level calculations [13] (dashed curves) in which the $D^{*\pm}$ is created from both color singlet and color octet contributions to the $(c\bar{q})$-state. The relative weight of these color configurations has been taken from comparisons of the BKL calculation to the published ZEUS D^* cross sections in photoproduction [14]. The calculation shows reasonable agreement with these DIS data.

Tables 2 and 3 give the resulting integrated cross sections binned in Q^2 and y for the $K2\pi$ and $K4\pi$ final states, respectively. The bin widths were chosen such that they contained of the order of 100 signal events. The resulting purity in each bin is better than 70%. The resolutions in both Q^2 and y are better than 10% in all bins. These bins were chosen to measure $F_2^{c\bar{c}}$ as described in the next section. Tables 2 and 3 also show the HVQDIS predictions for the different kinematic bins. The predictions are in good agreement with the data.

The quantitative agreement obtained between data and the HVQDIS calculation displayed in Fig. 5 and Tables 2 and 3 represents a confirmation of the hard scattering factorization theorem, in that the same gluon and three light-quark-flavor parton distributions describe both the ZEUS F_2 data and the $D^{*\pm}$ differential cross sections reported here. In view of the agreement observed here, the HVQDIS program can be used to extrapolate outside the accessible kinematic region to obtain the total $D^{*\pm}$ cross section.

10 Extraction of $F_2^{c\bar{c}}$

The charm contribution, $F_2^{c\bar{c}}$, to the proton structure function F_2 can be related to the double differential $c\bar{c}$ cross section in x and Q^2 by

$$\frac{d^2\sigma^{c\bar{c}}(x,Q^2)}{dxdQ^2} = \frac{2\pi\alpha^2}{xQ^4}\{[1+(1-y)^2]F_2^{c\bar{c}}(x,Q^2) - y^2F_L^{c\bar{c}}(x,Q^2)\}. \quad (4)$$

In this paper, the $c\bar{c}$ cross section is obtained by measuring the $D^{*\pm}$ production cross section and employing the hadronization fraction $f(c \to D^{*+})$ to derive the total charm cross section. Since only a limited kinematic region is accessible for the measurement of $D^{*\pm}$, a prescription for extrapolating to the full kinematic phase space is needed. The contribution of $F_L^{c\bar{c}}(x,Q^2)$ to the cross section in the measured Q^2, y region is estimated from the NLO theoretical prediction [45] to be less than 1% and is therefore neglected. Equation (4) defines $F_2^{c\bar{c}}$ as arising from events with one or more charm particles in the final state, but it is not a unique theoretical definition. It depends on the scheme and parton distributions [46].

In order to measure the contribution of charm to the inclusive F_2, the integrated cross sections in the Q^2 and y kinematic bins of Tables 2 and 3 were extrapolated to the full $p_T(D^*)$ and $\eta(D^*)$ phase space using HVQDIS with the RAPGAP-based fragmentation corrections discussed in the previous section. Typical extrapolation factors for the $K2\pi$ ($K4\pi$) final state were between 4 (10), at low Q^2, and 1.5 (4), at high Q^2. This procedure neglects the possibility of additional contributions outside the measured region due, for example, to intrinsic charm [47].

[3]Some double counting may occur between the NLO calculations and the parton shower, which contains resummed terms of all orders. This effect is estimated to be small from the calculations with the parton shower option in JETSET switched off.

The extrapolated cross sections are converted into $c\bar{c}$ cross sections using the hadronization fraction of charm to D^{*+}: $f(c \to D^{*+}) = 0.222 \pm 0.014 \pm 0.014$ [39]. The use of this value from OPAL implicitly assumes that charm production in DIS and e^+e^- annihilation produces the same fractions of the various charm final-states. The production of charm bound states, such as $e^+p \to e^+J/\psi X$, is not accounted for when using the LEP $c \to D^{*+}$ branching fraction. However, the inelastic J/ψ cross section has been calculated [48] to be only 2.5-4.5% of the total charm production cross section predicted by HVQDIS in the Q^2, y range of this analysis. The elastic J/ψ cross section has been measured in DIS [49] and is less than 0.5% of the predicted total charm cross section in the range of that measurement. The 9% uncertainty on the $c \to D^{*+}$ hadronization is larger than that arising from these J/ψ contributions, which have consequently been neglected.

The systematic uncertainty on the extrapolation of the measured $D^{*\pm}$ cross sections to the full $p_T(D^*)$ and $\eta(D^*)$ phase space was investigated: varying the parameter m_c by ± 0.15 GeV gave a variation which was typically <5%; using the standard Peterson fragmentation parameter $\epsilon = 0.035$ (instead of the RAPGAP fragmentation correction) yielded changes typically <15%; and using the GRV98HO pdf's in the NLO calculation generally caused changes of <20%. If these uncertainties are added in quadrature, they are typically smaller than the statistical errors. However, the fact that the data are measured in a small part of the available phase space means that a realistic uncertainty on the extrapolation cannot be evaluated. Therefore these extrapolation uncertainties are not included in the systematic uncertainties discussed below.

Since the structure function varies only slowly, it is assumed to be constant within a given Q^2 and y bin, so that the measured $F_2^{c\bar{c}}$ in a bin i is given by

$$F_{2\ meas}^{c\bar{c}}(x_i, Q_i^2) = \frac{\sigma_{i,meas}(e^+p \to D^*X)}{\sigma_{i,theor}(e^+p \to D^*X)} F_{2\ theor}^{c\bar{c}}(x_i, Q_i^2) \tag{5}$$

where the cross sections σ_i in bin i are those for the measured $p_T(D^*)$ and $\eta(D^*)$ region, and the subscripts *meas* and *theor* denote 'measured' and 'theoretical', respectively. The value of $F_{2\ theor}^{c\bar{c}}$ was calculated from the NLO coefficient functions [8], as implemented in a convenient parametrization [45]. The functional form of $F_{2\ theor}^{c\bar{c}}$ was used to quote the results for $F_2^{c\bar{c}}$ at convenient values of x_i and Q_i^2 close to the center-of-gravity of the bin. In this calculation, the same parton densities, charm mass (m_c= 1.4 GeV), and factorization and renormalization scales ($\sqrt{4m_c^2 + Q^2}$) have been used as for the HVQDIS calculation of the differential cross sections.

10.1 Combination of $F_2^{c\bar{c}}$ from both decays

Finally, the results from the two decay channels were combined in the eight common bins, taking into account all systematic uncertainties. The combined value is a weighted average with weights according to the statistical precision of the individual measurements. The systematic uncertainties were assumed to be either uncorrelated or 100% correlated between the analyses, as appropriate. All uncertainties concerning the DIS event selection were assumed to be correlated. Only the effect of the variation of the D^0 mass window and the changes in the p_T requirements for the D^0 decay products were taken as uncorrelated. As in both analyses, the positive and negative errors were treated separately. The procedure leads to a gain in statistical precision of 5-25%, compared to using only the $K2\pi$ decay channel.

10.2 Results and discussion

Table 4 and Fig. 7 display the $F_2^{c\bar{c}}$ values in the various Q^2 bins as a function of x. The structure function $F_2^{c\bar{c}}$ shows a rise with decreasing x at constant values of Q^2. The rise becomes steeper at higher Q^2.

The curves in Fig. 7 represent the results of the NLO QCD calculation [45] with the ZEUS NLO QCD pdf's. The central, solid curve corresponds to a charm quark mass of 1.4 GeV. Since good agreement was obtained between data and the HVQDIS calculation for the $D^{*\pm}$ differential cross sections and for the integrated cross sections shown in Tables 2 and 3 and since that calculation was used to extrapolate to the full kinematic range, the curves would be expected to describe the resulting values of $F_2^{c\bar{c}}$. The total uncertainty in the calculation of $F_2^{c\bar{c}}$, shown as the band of dashed curves around the solid curve, corresponds to the uncertainty propagated from the ZEUS NLO QCD fit and is dominated by the uncertainty in the charm quark mass, which was varied from 1.2 to 1.6 GeV.

Figure 8 shows $F_2^{c\bar{c}}$ at constant x values as a function of Q^2. Although the number of points is small, large scaling violations of the structure function are evident. The curves superimposed on the data are from the same calculation as shown in Fig. 7.

Figure 9 shows the ratio of $F_2^{c\bar{c}}$ to F_2, the inclusive proton structure function, as a function of x in fixed-Q^2 bins. The curves superimposed on the data are again from the calculation used for Fig. 7. The values of F_2 used to determine the ratio were taken from the ZEUS NLO QCD fit at the same Q^2 and x for which $F_2^{c\bar{c}}$ is quoted. The error on F_2 is negligible in comparison to $F_2^{c\bar{c}}$. The charm contribution to F_2 rises steeply with decreasing x. In the measured x region, $F_2^{c\bar{c}}$ accounts for $< 10\%$ of F_2 at low Q^2 and $x \simeq 5 \cdot 10^{-4}$ and rises to $\simeq 30\%$ of F_2 for $Q^2 > 11$ GeV^2 at the lowest x measured. The strong rise of $F_2^{c\bar{c}}$ at low values of x is similar to that of the gluon density and thus supports the hypothesis that charm production is dominated by the boson-gluon-fusion mechanism.

11 Summary

This paper presents an analysis of $D^{*\pm}$ production in DIS using the combined ZEUS 1996 and 1997 data samples with an integrated luminosity of 37 pb^{-1}, about ten times larger than in the previous ZEUS study. In addition, both the $K2\pi$ and $K4\pi$ decay modes of the D^* have been employed and their results combined. In the experimentally accessible region of 1.5 (2.5) $< p_T(D^*) <$15 GeV and $|\eta(D^*)| < 1.5$, the cross section for $D^{*\pm}$ production for the $K2\pi$ ($K4\pi$) final state in events with $1 < Q^2 < 600$ GeV^2 and $0.02 < y < 0.7$ is $8.31 \pm 0.31(\text{stat})^{+0.30}_{-0.50}(\text{sys})$ nb ($3.65 \pm 0.36(\text{stat})^{+0.20}_{-0.41}(\text{sys})$ nb).

QCD calculations of charm production based on the NLO boson-gluon-fusion process with three flavors of light quarks show excellent agreement with the overall cross section and with the Q^2 and y distributions. The $\eta(D^*)$ and $x(D^*)$ distributions, however, cannot be reproduced with the standard Peterson fragmentation. Good agreement is obtained after a more appropriate $c \to D^{*+}$ fragmentation, such as that in JETSET, is used.

The quantitative agreement between the NLO pQCD calculations and the ZEUS data provides a confirmation of the hard scattering factorization theorem, whereby the same gluon density in the proton describes both the inclusive F_2 and the DIS production of charm.

The charm contribution, $F_2^{c\bar{c}}$, to the proton structure function F_2 was obtained using the NLO QCD calculation to extrapolate outside the measured $p_T(D^*)$ and $\eta(D^*)$ region. Compared to the previous ZEUS study, the kinematic range has been extended down to $Q^2 = 1.8$ GeV^2 and

up to $Q^2 = 130$ GeV^2, with reduced uncertainties. The structure function $F_2^{c\bar{c}}$ exhibits large scaling violations, as well as a steep rise with decreasing x at constant Q^2. For $Q^2 > 11$ GeV^2 and $x \simeq 10^{-3}$, the ratio of $F_2^{c\bar{c}}$ to F_2 is about 0.3.

12 Acknowledgements

We thank the DESY Directorate for their strong support and encouragement. The remarkable achievements of the HERA machine group were essential for the successful completion of this work and are gratefully appreciated. We also acknowledge the many informative discussions we have had with J. Amundson, A. Berezhnoy, J. Collins, S. Fleming, B. Harris, F. Olness, C. Schmidt, J. Smith, W.K. Tung and A. Vogt.

References

[1] H1 Collab., C. Adloff *et al.*, Z. Phys. C**72**, 593 (1996)

[2] ZEUS Collab., J. Breitweg *et al.*, Phys. Lett. B**407**, 402 (1997)

[3] EMC Collab., J. J. Aubert *et al.*, Nucl. Phys. B**213**, 31 (1983)

[4] H1 Collab., C. Adloff *et al.*, Nucl. Phys. B **545**, 21 (1999)

[5] S. Nussinov, Phys. Rev. Lett. **35**, 1672 (1975)

[6] B. W. Harris and J. Smith, Phys. Rev. D**57**, 2806 (1998)

[7] B. W. Harris and J. Smith, Nucl. Phys. B**452**, 109 (1995); Phys. Lett. B**353**, 535 (1995)

[8] E. Laenen *et al.*, Nucl. Phys. B**392**, 162 (1993); ibid., B**392**, 229 (1993)

[9] M. A. G. Aivazis *et al.*, Phys. Rev. D**50**, 3102 (1994)

[10] M. Buza *et al.*, Phys. Lett. B**411**, 211 (1997)

[11] J. C. Collins, Phys. Rev. D**58**, 094002 (1998)

[12] A. D. Martin *et al.*, Eur. Phys. J. C**4**, 463 (1998)

[13] A. V. Berezhnoy, V. V. Kiselev and A. K. Likhoded, hep-ph/9901333 v2 (1999) and hep-ph/9905555 (1999)

[14] ZEUS Collab., J. Breitweg *et al.*, Eur. Phys. J. C**6**, 67 (1999)

[15] ZEUS Collab., M. Derrick *et al.*, The ZEUS Detector, Status Report 1993, DESY (1993)

[16] N. Harnew *et al.*, Nucl. Instr. and Meth. A**279**, 290 (1989);
B. Foster *et al.*, Nucl. Phys. B (Proc. Suppl.) **32**, 181 (1993);
B. Foster *et al.*, Nucl. Instr. and Meth. A**338**, 254 (1994)

[17] M. Derrick *et al.*, Nucl. Instr. and Meth. A**309**, 77 (1991);
A. Andresen *et al.*, ibid., 101 (1991);
A. Caldwell *et al.*, ibid. A**321**, 356 (1992);
A. Bernstein *et al.*, ibid. A**336**, 23 (1993)

[18] A. Bamberger *et al.*, Nucl. Instr. and Meth. A**401**, 63 (1997)

[19] J. Andruszków *et al.*, DESY 92-066 (1992)

[20] H. Abramowicz, A. Caldwell and R. Sinkus, Nucl. Instr. and Meth. A**365**, 508 (1995)

[21] ZEUS Collab., M. Derrick *et al.*, Eur. Phys. J. C**1**, 81 (1998); ibid. C**6**, 43 (1999)

[22] G. Briskin, PhD Thesis, University of Tel Aviv, (1998) unpublished

[23] S. Bentvelsen, J. Engelen, and P. Kooijman, Proc. of the 1991 Workshop on Physics at HERA, DESY, Hamburg, Vol. 1 (1992) p. 23

[24] U. Bassler and G. Bernardi, Nucl. Instr. and Meth. A**361**, 197 (1995)

[25] ZEUS Collab., M. Derrick *et al.*, Z. Phys. C**67**, 93 (1995)

[26] R. Brun *et al.*, CERN DD/EE/84-1 (1987)

[27] H. Jung, Comp. Phys. Comm. **86**, 147 (1995)

[28] A. Kwiatkowski, H. Spiesberger and H.-J. Möhring, Proc. of the 1991 Workshop on Physics at HERA, DESY, Hamburg, Vol. 3 (1992), p. 1294; Z. Phys. C**50**, 165 (1991)

[29] M. Glück, E. Reya and A. Vogt, Z. Phys. C**67**, 433 (1995)

[30] B. Andersson *et al.*, Phys. Rep. **97**, 31 (1983)

[31] T. Sjöstrand, Comp. Phys. Comm. **82**, 74 (1994)

[32] C. Peterson *et al.*, Phys. Rev. D**27**, 105 (1983)

[33] OPAL Collab., R. Akers *et al.*, Z. Phys. C**67**, 27 (1995)

[34] G. Marchesini *et al.*, Comp. Phys. Comm. **67**, 465 (1992)

[35] W. H. Smith *et al.*, Nucl. Instr. and Meth. A**355**, 278 (1995)

[36] ZEUS Collab., J. Breitweg *et al.*, Eur. Phys. J. C**7** 609 (1999)

[37] Particle Data Group, C. Caso *et al.*, Eur. Phys. J. C**3**, 1 (1998)

[38] R. Hall-Wilton, PhD Thesis, University of Bristol, (1999) unpublished

[39] OPAL Collab., K. Ackerstaff *et al.*, Eur. Phys. J. C**1**, 439 (1998)

[40] ZEUS Collab., 'Open Charm Production in Deep Inelastic Diffractive Scattering at HERA', Contribution No. 785, ICHEP98, Vancouver, July 23-29, 1998

[41] The result of the ZEUS NLO QCD fit is described in [36]. New fits were made using various charm masses

[42] M. Glück, E. Reya and A. Vogt, Eur. Phys. J. C**5**, 461 (1998)

[43] S. Frixione *et al.*, Nucl. Phys. B**412**, 225 (1994)

[44] E. Norrbin and T. Sjöstrand, hep-ph/9905493

[45] S. Riemersma, J. Smith and W. L. Van Neerven, Phys. Lett. B**347**, 143 (1995)

[46] CTEQ Collab., H. Lai et al., hep-ph/9903282

[47] S. J. Brodsky *et al.*, Phys. Lett. **93**B, 451 (1980)

[48] S. Fleming and T. Mehen, Phys. Rev. D**57**, 1846 (1998) and private communication

[49] ZEUS Collab., J. Breitweg *et al.*, Eur. Phys. J. C**6**, 603 (1999)

Table 1: *The $D^* \to K\pi\pi_s$ and $D^* \to K\pi\pi\pi\pi_s$ differential cross sections. The bin range, the center-of-gravity of the bin (see text) and the cross sections for all the data in Figs. 5 and 6 are shown. The first error is the statistical error and the asymmetric errors are the statistical and systematic uncertainties added in quadrature. The overall normalization uncertainties arising from the luminosity measurement (±1.65%) and from the $D^{*\pm}$ and D^0 decay branching ratios are not included.*

$K\pi\pi_s$		$K\pi\pi_s$	
(range) $log_{10}(Q^2)$	$d\sigma/dlog_{10}(Q^2)$ (nb)	(range) $log_{10}(x)$	$d\sigma/dlog_{10}(x)$ (nb)
(0.0,0.7) 0.39	$5.99 \pm 0.47\ ^{+0.61}_{-0.74}$	(-4.1,-3.4) -3.69	$4.54 \pm 0.35\ ^{+0.45}_{-0.56}$
(0.7,1.0) 0.85	$5.17 \pm 0.39\ ^{+0.54}_{-0.46}$	(-3.4,-2.8) -3.08	$4.24 \pm 0.23\ ^{+0.34}_{-0.27}$
(1.0,1.3) 1.16	$4.50 \pm 0.33\ ^{+0.43}_{-0.44}$	(-2.8,-2.3) -2.56	$2.06 \pm 0.16\ ^{+0.19}_{-0.17}$
(1.3,1.6) 1.45	$2.72 \pm 0.25\ ^{+0.32}_{-0.29}$	(-2.3,-2.0) -2.16	$0.78 \pm 0.14\ ^{+0.15}_{-0.16}$
(1.6,1.9) 1.74	$1.47 \pm 0.17\ ^{+0.18}_{-0.17}$	(-2.0,-1.5) -1.82	$0.25 \pm 0.10\ ^{+0.11}_{-0.09}$
(1.9,2.3) 2.08	$0.47 \pm 0.08\ ^{+0.11}_{-0.10}$		
(2.3,2.8) 2.48	$0.135 \pm 0.073\ ^{+0.096}_{-0.069}$		

$K\pi\pi_s$		$K\pi\pi_s$	
(range) W (GeV)	$d\sigma/dW$ (nb/GeV)	(range) $x(D^*)$	$d\sigma/dx(D^*)$ (nb)
(50,90) 73	$0.0450 \pm 0.0035^{+0.0047}_{-0.0079}$	(0.0,0.2) 0.13	$9.3 \pm 1.2\ ^{+1.4}_{-2.2}$
(90,115) 102	$0.0659 \pm 0.0048^{+0.0074}_{-0.0068}$	(0.2,0.3) 0.28	$13.2 \pm 1.2\ ^{+1.9}_{-1.4}$
(115,145) 129	$0.0510 \pm 0.0039^{+0.0068}_{-0.0059}$	(0.3,0.5) 0.42	$13.61 \pm 0.98\ ^{+1.22}_{-1.90}$
(145,175) 159	$0.0442 \pm 0.0038^{+0.0059}_{-0.0049}$	(0.5,0.6) 0.55	$12.79 \pm 1.03\ ^{+1.49}_{-0.99}$
(175,200) 187	$0.0361 \pm 0.0043^{+0.0067}_{-0.0071}$	(0.6,0.8) 0.67	$8.15 \pm 0.60\ ^{+0.95}_{-1.24}$
(200,250) 222	$0.0266 \pm 0.0032^{+0.0033}_{-0.0069}$	(0.8,1.0) 0.80	$1.12 \pm 0.10\ ^{+0.27}_{-0.27}$

$K\pi\pi_s$		$K\pi\pi\pi\pi_s$	
(range) $p_T(D^*)$ (GeV)	$d\sigma/dp_T(D^*)$ (nb/GeV)	(range) $p_T(D^*)$ (GeV)	$d\sigma/dp_T(D^*)$ (nb/GeV)
(1.5,2.4) 1.91	$3.82 \pm 0.39\ ^{+0.48}_{-0.65}$	(2.5,3.0) 2.74	$2.42 \pm 0.76\ ^{+0.90}_{-0.97}$
(2.4,3.1) 2.72	$2.72 \pm 0.21\ ^{+0.26}_{-0.28}$	(3.0,3.5) 3.24	$1.63 \pm 0.49\ ^{+1.4}_{-0.71}$
(3.1,4.0) 3.50	$1.57 \pm 0.10\ ^{+0.14}_{-0.13}$	(3.5,4.0) 3.73	$1.03 \pm 0.29\ ^{+0.52}_{-0.33}$
(4.0,6.0) 4.77	$0.527 \pm 0.033\ ^{+0.041}_{-0.047}$	(4.0,6.0) 4.74	$0.43 \pm 0.06\ ^{+0.31}_{-0.07}$
(6.0,15.0) 7.93	$0.0419 \pm 0.0034^{+0.0043}_{-0.0041}$	(6.0,8.0) 6.77	$0.127 \pm 0.019^{+0.074}_{-0.026}$
		(8.0,10.0) 8.75	$0.044 \pm 0.010^{+0.022}_{-0.010}$
		(10.0,15.0) 11.73	$0.007 \pm 0.002^{+0.011}_{-0.003}$

$K\pi\pi_s$		$K\pi\pi\pi\pi_s$	
(range) $\eta(D^*)$	$d\sigma/d\eta(D^*)$ (nb)	(range) $\eta(D^*)$	$d\sigma/d\eta(D^*)$ (nb)
(-1.5,-0.8) -1.13	$1.93 \pm 0.19\ ^{+0.27}_{-0.29}$	(-1.5,-1.0) -1.18	$0.73 \pm 0.21\ ^{+0.22}_{-0.31}$
(-0.8,-0.4) -0.58	$2.41 \pm 0.21\ ^{+0.22}_{-0.25}$	(-1.0,-0.5) -0.73	$1.03 \pm 0.23\ ^{+0.16}_{-0.21}$
(-0.3,0.0) -0.18	$3.04 \pm 0.28\ ^{+0.30}_{-0.37}$	(-0.5,0.0) -0.24	$1.48 \pm 0.26\ ^{+0.23}_{-0.27}$
(0.0,0.4) 0.20	$3.09 \pm 0.25\ ^{+0.30}_{-0.31}$	(0.0,0.5) 0.26	$1.48 \pm 0.31\ ^{+0.42}_{-0.27}$
(0.4,0.8) 0.60	$3.15 \pm 0.27\ ^{+0.38}_{-0.43}$	(0.5,1.0) 0.75	$1.12 \pm 0.35\ ^{+0.34}_{-0.44}$
(0.8,1.5) 1.15	$3.26 \pm 0.31\ ^{+0.40}_{-0.44}$	(1.0,1.5) 1.22	$2.08 \pm 0.45\ ^{+0.81}_{-0.78}$

Table 2: *The cross sections for $D^{*\pm}$ production from the $K2\pi$ final state. The table contains for each bin: the Q^2 range of the bin; the y range of the bin; the measured $D^{*\pm}$ cross section in the bin with statistical and systematic uncertainties; and the HVQDIS prediction for this cross section. The overall normalization uncertainties arising from the luminosity measurement ($\pm 1.65\%$) and from the $D^{*\pm}$ and D^0 decay branching ratios are not included.*

Q^2 range (GeV^2)	y range	$\sigma(D^*)$ meas. (nb)	$\sigma(D^*)$ pred.(nb)
1–3.5	0.70–0.24	$1.45 \pm 0.23^{+0.20}_{-0.22}$	1.12
	0.24–0.11	$1.00 \pm 0.20^{+0.17}_{-0.17}$	1.00
	0.11–0.02	$0.92 \pm 0.16^{+0.15}_{-0.91}$	1.10
3.5–6.5	0.70–0.22	$0.73 \pm 0.10^{+0.07}_{-0.11}$	0.54
	0.22–0.11	$0.342 \pm 0.055^{+0.068}_{-0.036}$	0.405
	0.11–0.02	$0.433 \pm 0.066^{+0.069}_{-0.076}$	0.528
6.5–9	0.70–0.15	$0.388 \pm 0.060^{+0.051}_{-0.053}$	0.369
	0.15–0.02	$0.288 \pm 0.046^{+0.068}_{-0.008}$	0.355
9–14	0.70–0.23	$0.370 \pm 0.057^{+0.038}_{-0.030}$	0.302
	0.23–0.11	$0.314 \pm 0.045^{+0.051}_{-0.076}$	0.251
	0.11–0.02	$0.253 \pm 0.042^{+0.011}_{-0.020}$	0.316
14–22	0.70–0.23	$0.25 \pm 0.05^{+0.11}_{-0.02}$	0.26
	0.23–0.11	$0.254 \pm 0.043^{+0.044}_{-0.073}$	0.212
	0.11–0.02	$0.226 \pm 0.035^{+0.052}_{-0.027}$	0.250
22–44	0.70–0.23	$0.387 \pm 0.053^{+0.052}_{-0.040}$	0.301
	0.23–0.11	$0.200 \pm 0.027^{+0.028}_{-0.021}$	0.226
	0.70–0.23	$0.198 \pm 0.033^{+0.031}_{-0.018}$	0.240
44–90	0.23–0.02	$0.202 \pm 0.043^{+0.050}_{-0.019}$	0.188
	0.23–0.70	$0.200 \pm 0.032^{+0.011}_{-0.016}$	0.221
90–200	0.70–0.23	$0.090 \pm 0.023^{+0.086}_{-0.013}$	0.099
	0.23–0.02	$0.075 \pm 0.015^{+0.010}_{-0.007}$	0.086

Table 3: *The cross sections for $D^{*\pm}$ production from the $K4\pi$ final state. The table contains for each bin: the Q^2 range of the bin; the y range of the bin; the measured $D^{*\pm}$ cross section in the bin with statistical and systematic uncertainties; and the HVQDIS prediction for this cross section. The overall normalization uncertainties arising from the luminosity measurement ($\pm 1.65\%$) and from the $D^{*\pm}$ and D^0 decay branching ratios are not included.*

Q^2 range (GeV^2)	y range	$\sigma(D^*)$ meas. (nb)	$\sigma(D^*)$ pred. (nb)
1–10	0.70–0.34	$0.94 \pm 0.29^{+0.39}_{-0.21}$	0.61
	0.34–0.02	$1.39 \pm 0.51^{+0.21}_{-0.92}$	1.55
10–21	0.70–0.28	$0.35 \pm 0.08^{+0.11}_{-0.06}$	0.21
	0.28–0.02	$0.59 \pm 0.11^{+0.07}_{-0.11}$	0.47
21–33	0.70–0.22	$0.115 \pm 0.055^{+0.039}_{-0.023}$	0.154
	0.22–0.02	$0.125 \pm 0.045^{+0.048}_{-0.050}$	0.209
50–600	0.70–0.22	$0.23 \pm 0.07^{+0.07}_{-0.13}$	0.249
	0.22–0.02	$0.240 \pm 0.061^{+0.059}_{-0.084}$	0.221

Table 4: *The $F_2^{c\bar{c}}$ results derived from the combination of the $K2\pi$ and $K4\pi$ channels (see text). The table contains for each bin: the Q^2 value at which $F_2^{c\bar{c}}$ is reported; the x value at which $F_2^{c\bar{c}}$ is reported; and the measured $F_2^{c\bar{c}}$ with statistical and systematic uncertainties. The overall normalization uncertainties arising from the luminosity measurement ($\pm 1.65\%$), the $D^{*\pm}$ and D^0 decay branching ratios, the charm hadronization fraction to D^{*+} ($\pm 9\%$) and the extrapolation uncertainties (see text) are not included.*

Q^2 (GeV^2)	x	$F_2^{c\bar{c}}(x,Q^2)$ meas. $\pm$stat. $\pm$ syst.
1.8	$5.0 \cdot 10^{-5}$	$0.107 \pm 0.017^{+0.015}_{-0.016}$
	$1.3 \cdot 10^{-4}$	$0.054 \pm 0.011^{+0.009}_{-0.009}$
	$5.0 \cdot 10^{-4}$	$0.034 \pm 0.006^{+0.005}_{-0.003}$
4	$1.3 \cdot 10^{-4}$	$0.195 \pm 0.024^{+0.018}_{-0.028}$
	$3.0 \cdot 10^{-4}$	$0.088 \pm 0.013^{+0.015}_{-0.008}$
	$1.2 \cdot 10^{-3}$	$0.058 \pm 0.009^{+0.009}_{-0.010}$
7	$3.0 \cdot 10^{-4}$	$0.176 \pm 0.027^{+0.023}_{-0.024}$
	$1.2 \cdot 10^{-3}$	$0.095 \pm 0.015^{+0.023}_{-0.002}$
11	$3.0 \cdot 10^{-4}$	$0.314 \pm 0.048^{+0.032}_{-0.025}$
	$8.0 \cdot 10^{-4}$	$0.211 \pm 0.030^{+0.035}_{-0.051}$
	$2.0 \cdot 10^{-3}$	$0.123 \pm 0.020^{+0.006}_{-0.010}$
18	$5.0 \cdot 10^{-4}$	$0.32 \pm 0.05^{+0.11}_{-0.03}$
	$1.2 \cdot 10^{-3}$	$0.248 \pm 0.031^{+0.028}_{-0.044}$
	$4.0 \cdot 10^{-3}$	$0.136 \pm 0.021^{+0.031}_{-0.017}$
30	$8.0 \cdot 10^{-4}$	$0.395 \pm 0.052^{+0.050}_{-0.037}$
	$2.0 \cdot 10^{-3}$	$0.181 \pm 0.024^{+0.025}_{-0.021}$
	$8.0 \cdot 10^{-3}$	$0.121 \pm 0.021^{+0.019}_{-0.011}$
60	$2.0 \cdot 10^{-3}$	$0.361 \pm 0.077^{+0.090}_{-0.033}$
	$8.0 \cdot 10^{-3}$	$0.168 \pm 0.027^{+0.009}_{-0.013}$
130	$4.0 \cdot 10^{-3}$	$0.272 \pm 0.053^{+0.039}_{-0.067}$
	$2.0 \cdot 10^{-2}$	$0.109 \pm 0.017^{+0.014}_{-0.017}$

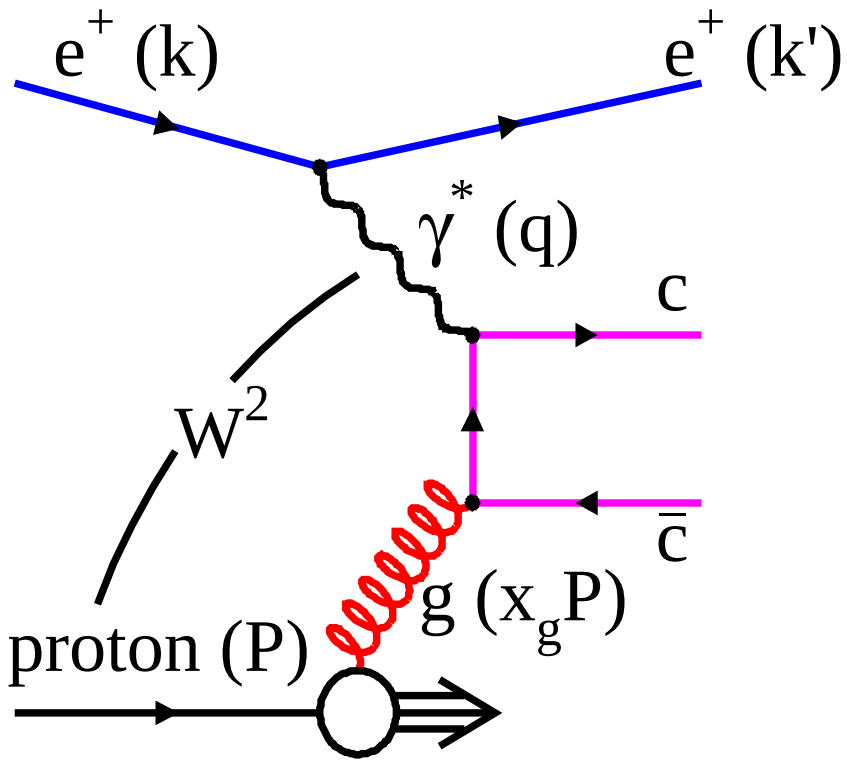

Figure 1: *Diagram of the boson-gluon-fusion process in e^+p collisions.*

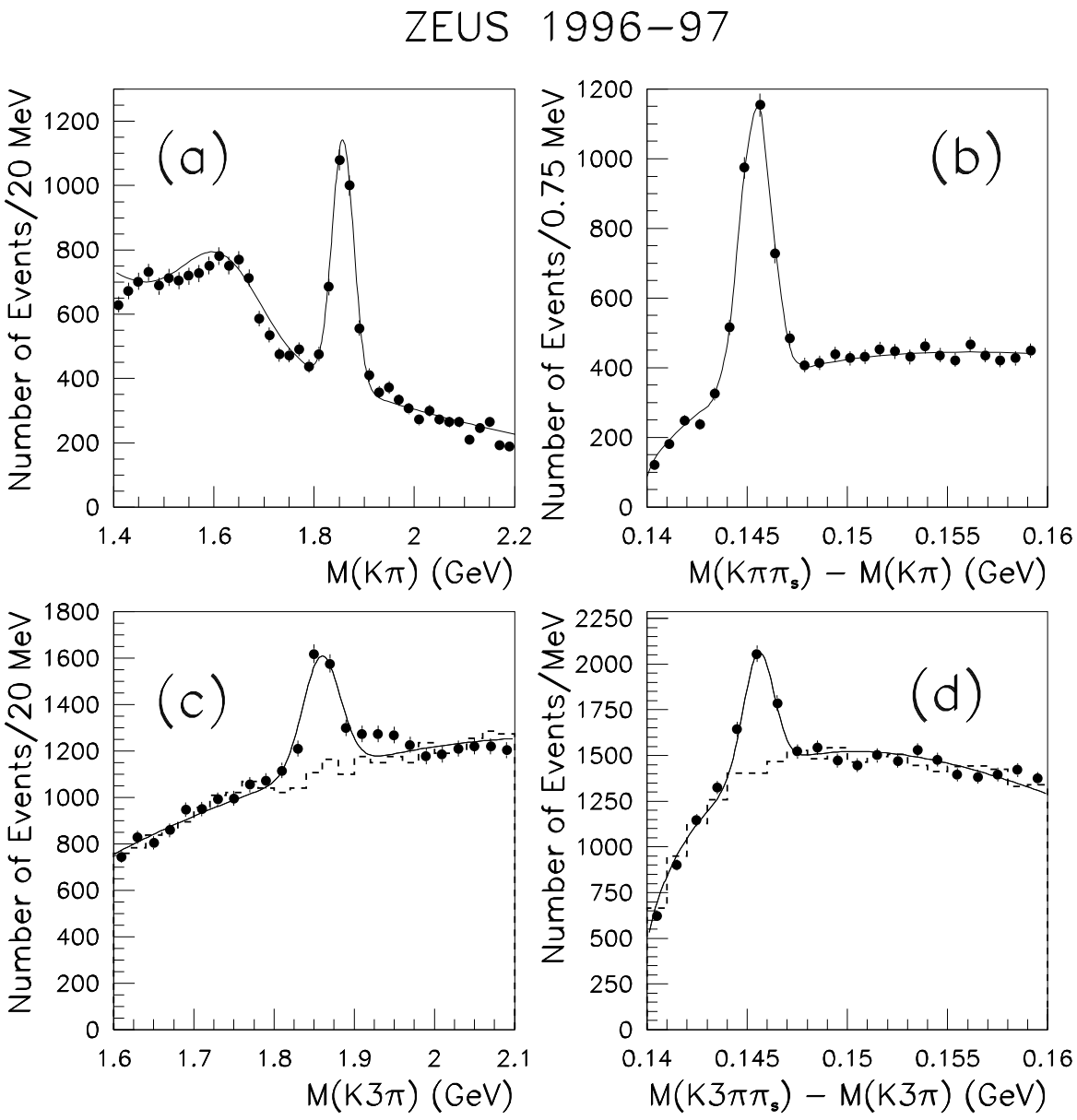

Figure 2: *ZEUS data in the kinematic region* $1 < Q^2 < 600$ GeV^2 *and* $0.02 < y < 0.7$*: (a)* $M(D^0) = M(K\pi)$ *and (b)* $\Delta M = M(K\pi\pi_s) - M(K\pi)$ *for the* $K2\pi$ *final state. The data are shown in the same kinematic region for the* $K4\pi$ *final state in (c)* $M(D^0) = M(K3\pi)$ *and (d)* $\Delta M = M(K3\pi\pi_s) - M(K3\pi)$*. The events in (a) and (c) are those for which 143 <* ΔM *< 148* MeV*. Similarly, (b) and (d) are shown for events in the* $M(D^0)$ *signal region: 1.80-1.92 (1.81-1.91)* GeV *for the* $K2\pi$ *(*$K4\pi$*) channel. The solid curves are the results of the fits described in the text. The dashed histograms in (c) and (d) represent the background distributions obtained by restricting the sample to side-bands from the* ΔM *and* $M(D^0)$ *distributions, respectively.*

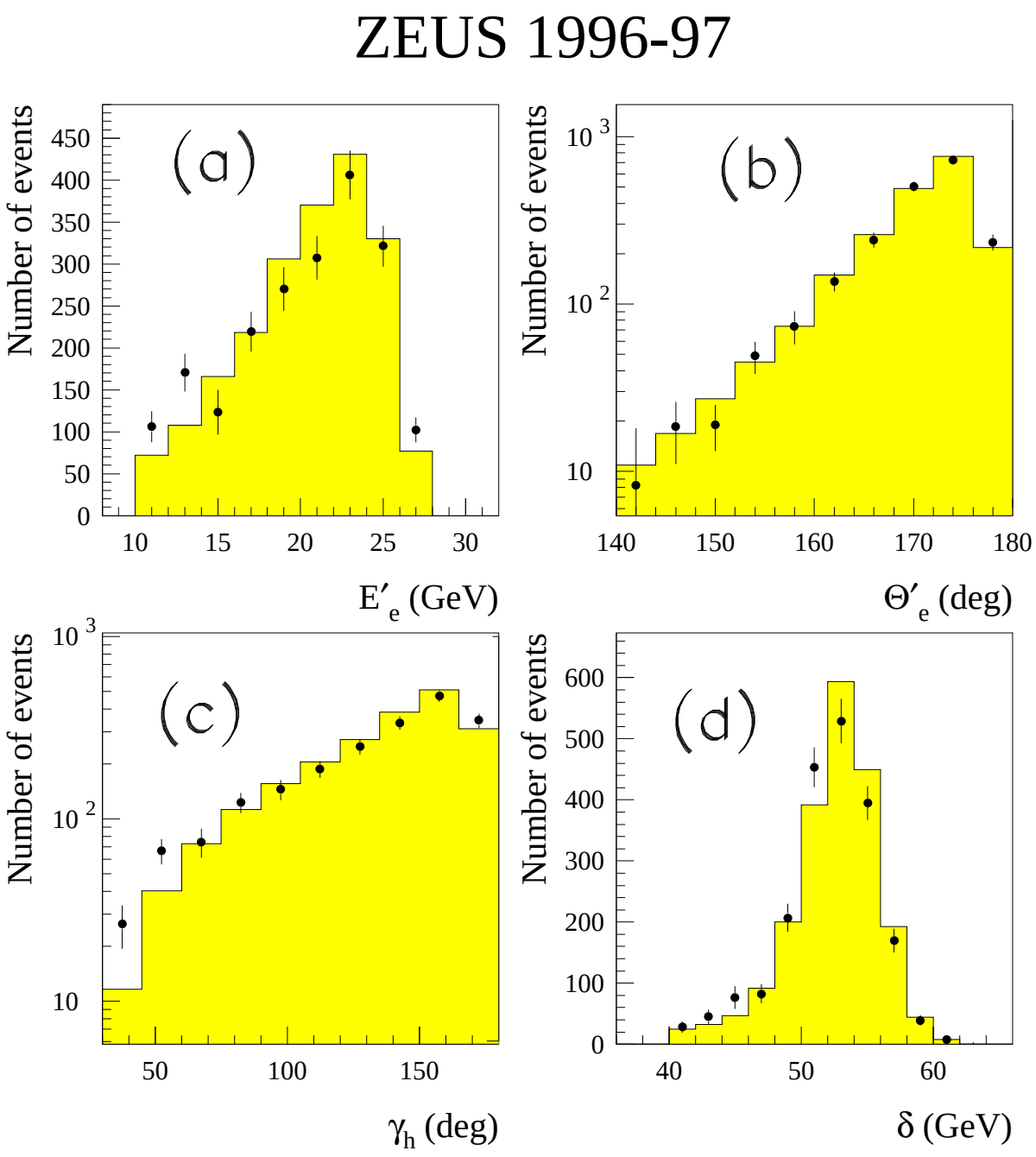

Figure 3: *A comparison of reconstructed DIS quantities at the detector level for the K2π data (points) and for the RAPGAP Monte Carlo simulation (shaded histogram): (a) the scattered positron energy, E'_e, (b) the scattered positron angle, θ'_e, (c) the hadronic angle, γ_h and (d) $\delta \equiv \Sigma_i (E_i - p_{z,i})$.*

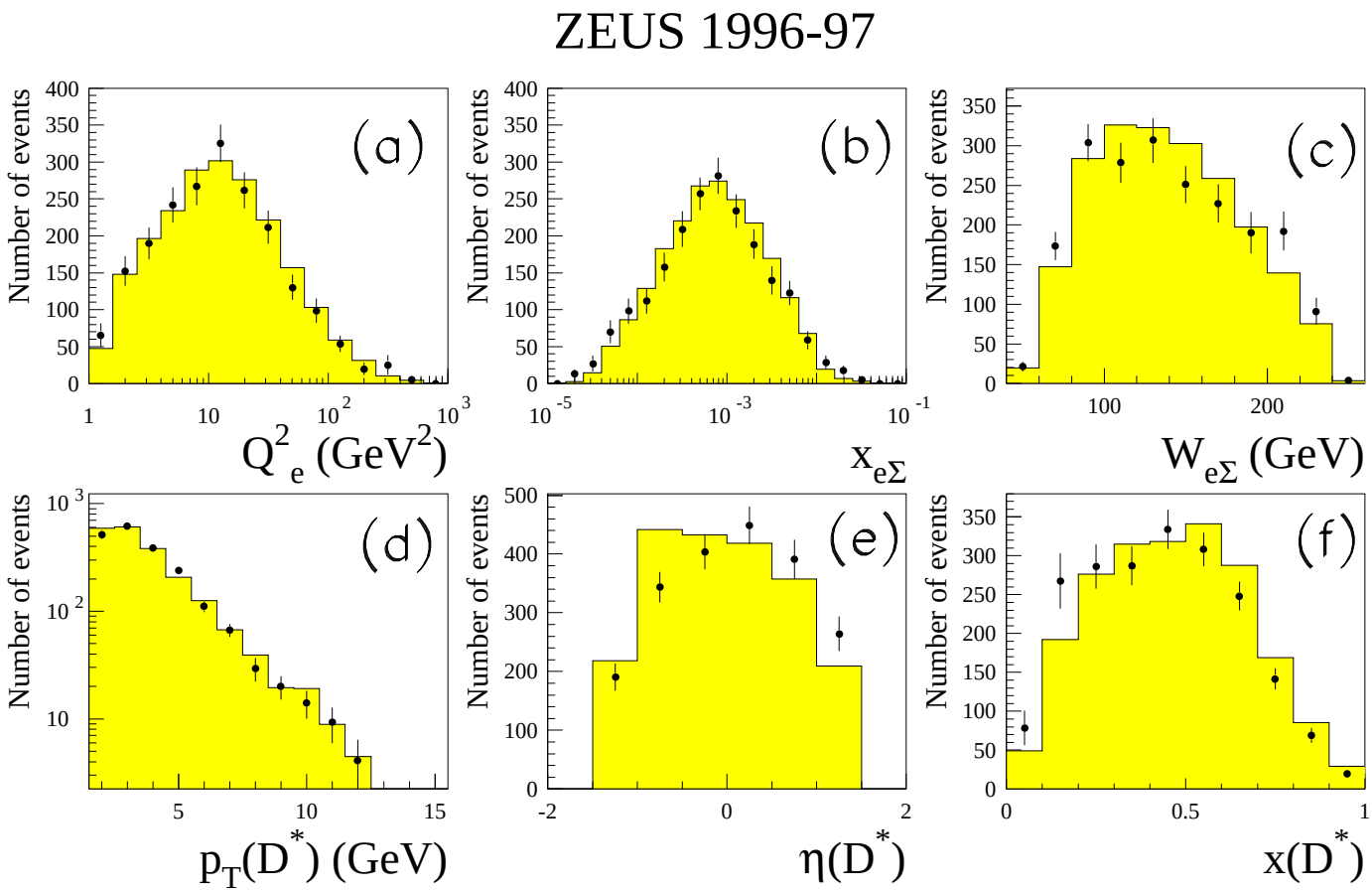

Figure 4: *A comparison of the reconstructed DIS kinematic distributions at the detector level for the $K2\pi$ data (points) and for the RAPGAP Monte Carlo simulation (shaded histogram): (a) Q^2_e, (b) Bjorken-x, $x_{e\Sigma}$ and (c) the total hadronic center-of-mass energy, $W_{e\Sigma}$. The remaining plots show a comparison of the reconstructed $D^{*\pm}$-related quantities at the detector level for data and for the RAPGAP Monte Carlo simulation: (d) $p_T(D^*)$, (e) $\eta(D^*)$ and (f) $x(D^*)$.*

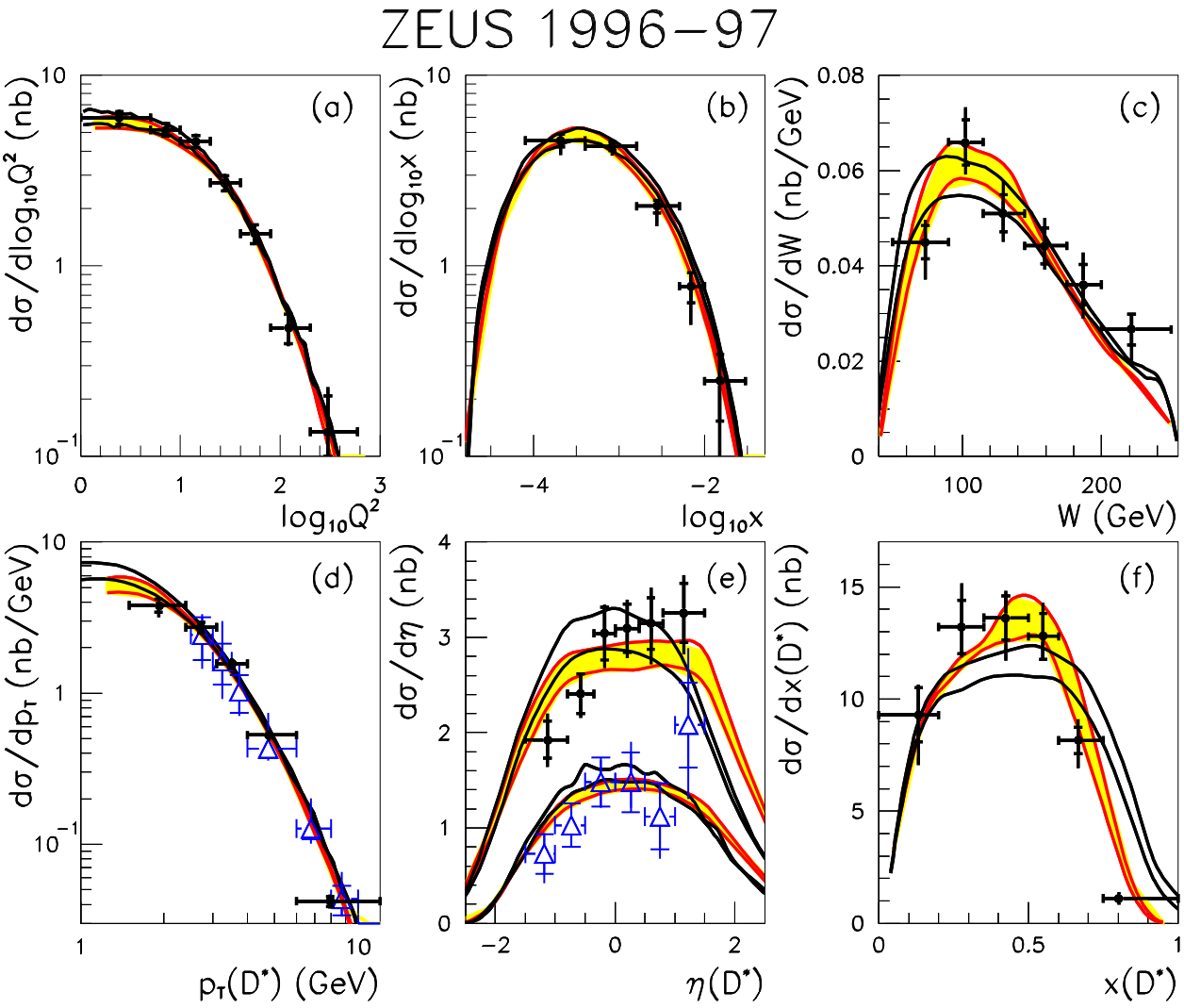

Figure 5: *Differential cross sections for $D^{*\pm}$ production from the $K2\pi$ final state (solid dots) in the Q^2, y, $p_T(D^*)$ and $\eta(D^*)$ kinematic region as functions of (a) $\log_{10} Q^2$, (b) $\log_{10} x$, (c) W, (d) $p_T(D^*)$, (e) $\eta(D^*)$ and (f) $x(D^*)$. The inner error bars show the statistical uncertainties while the outer ones show the statistical and systematic uncertainties summed in quadrature. The results from the $K4\pi$ channel (open triangles) are also shown in the $p_T(D^*)$(d) and $\eta(D^*)$ (e) plots. The data are compared with the NLO QCD calculation as implemented in HVQDIS using the ZEUS NLO pdf's. The open band corresponds to the standard Peterson fragmentation function with the parameter $\epsilon = 0.035$. For the shaded band, the Peterson fragmentation was replaced by that extracted from RAPGAP (see the text for details). The boundaries of the bands correspond to charm mass variations between 1.3 (upper curve) and 1.5* GeV *(lower curve). In (a) and (b), the open band is indistinguishable from the shaded band.*

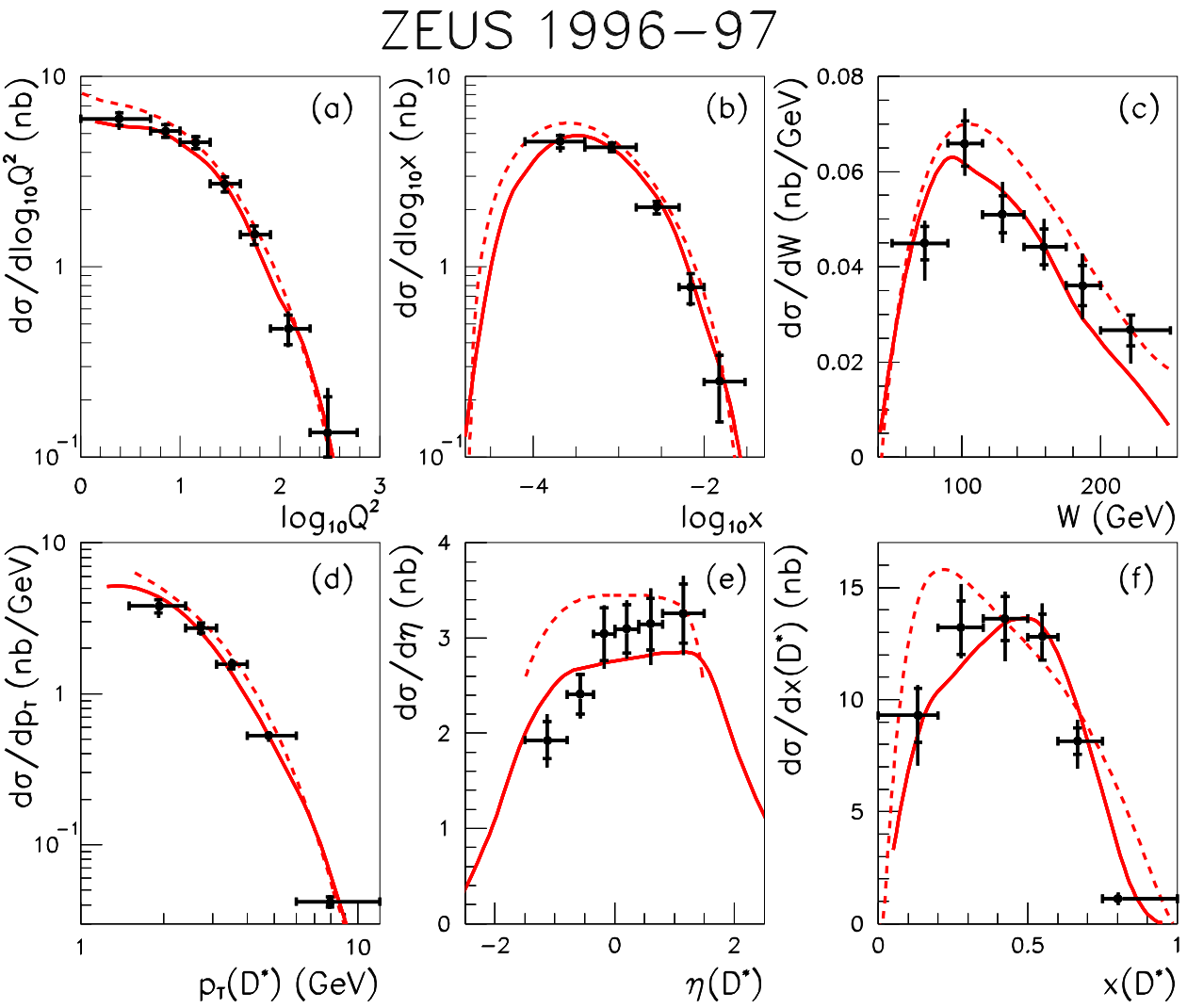

Figure 6: *Differential cross sections for $D^{*\pm}$ production from the $K2\pi$ final state (solid dots) in the accessible Q^2, y, $p_T(D^*)$ and $\eta(D^*)$ region as functions of (a) $\log_{10} Q^2$, (b) $\log_{10} x$, (c) W, (d) $p_T(D^*)$, (e) $\eta(D^*)$ and (f) $x(D^*)$. The inner error bars show the statistical uncertainties while the outer ones show the statistical and systematic uncertainties summed in quadrature. The solid curves show the results of the HVQDIS calculation with RAPGAP-based fragmentation and $m_c = 1.4$* GeV *while the dashed curves correspond to the BKL results (see text).*

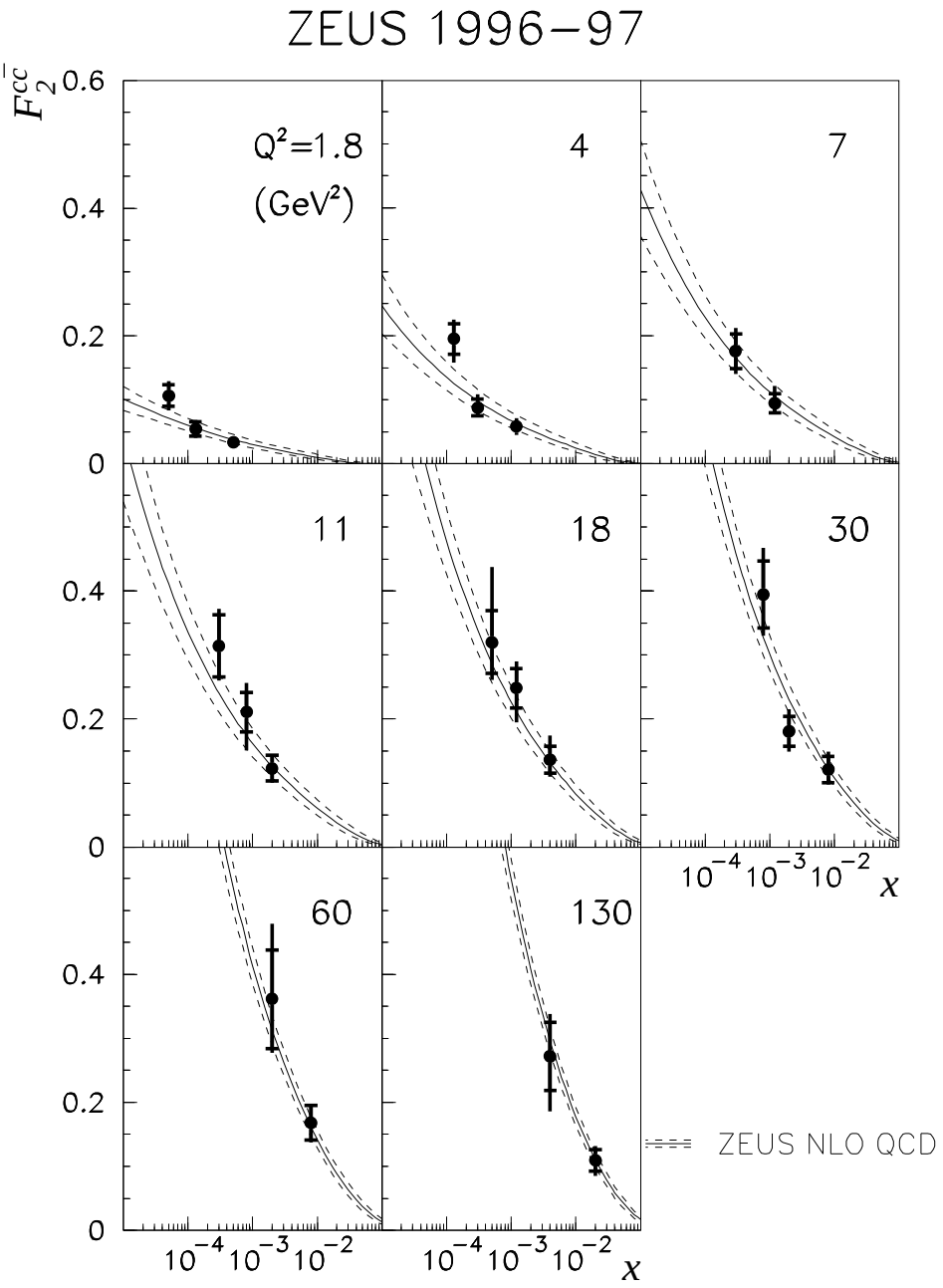

Figure 7: *The measured $F_2^{c\bar{c}}$ at Q^2 values between 1.8 and 130* GeV^2 *as a function of x. The inner error bars show the statistical uncertainty and the outer ones show the statistical and experimental systematic uncertainties summed in quadrature. The curves correspond to the NLO QCD calculation [7, 45] using the result of the ZEUS NLO QCD fit to F_2 [41]. The solid curves correspond to the central values and the dashed curves give the uncertainty due to the parton distributions from the ZEUS NLO fit. The overall normalization uncertainties arising from the luminosity measurement ($\pm 1.65\%$), the $D^{*\pm}$ and D^0 decay branching ratios, the charm hadronization fraction to D^{*+} ($\pm 9\%$) and the extrapolation uncertainties (see text) are not included.*

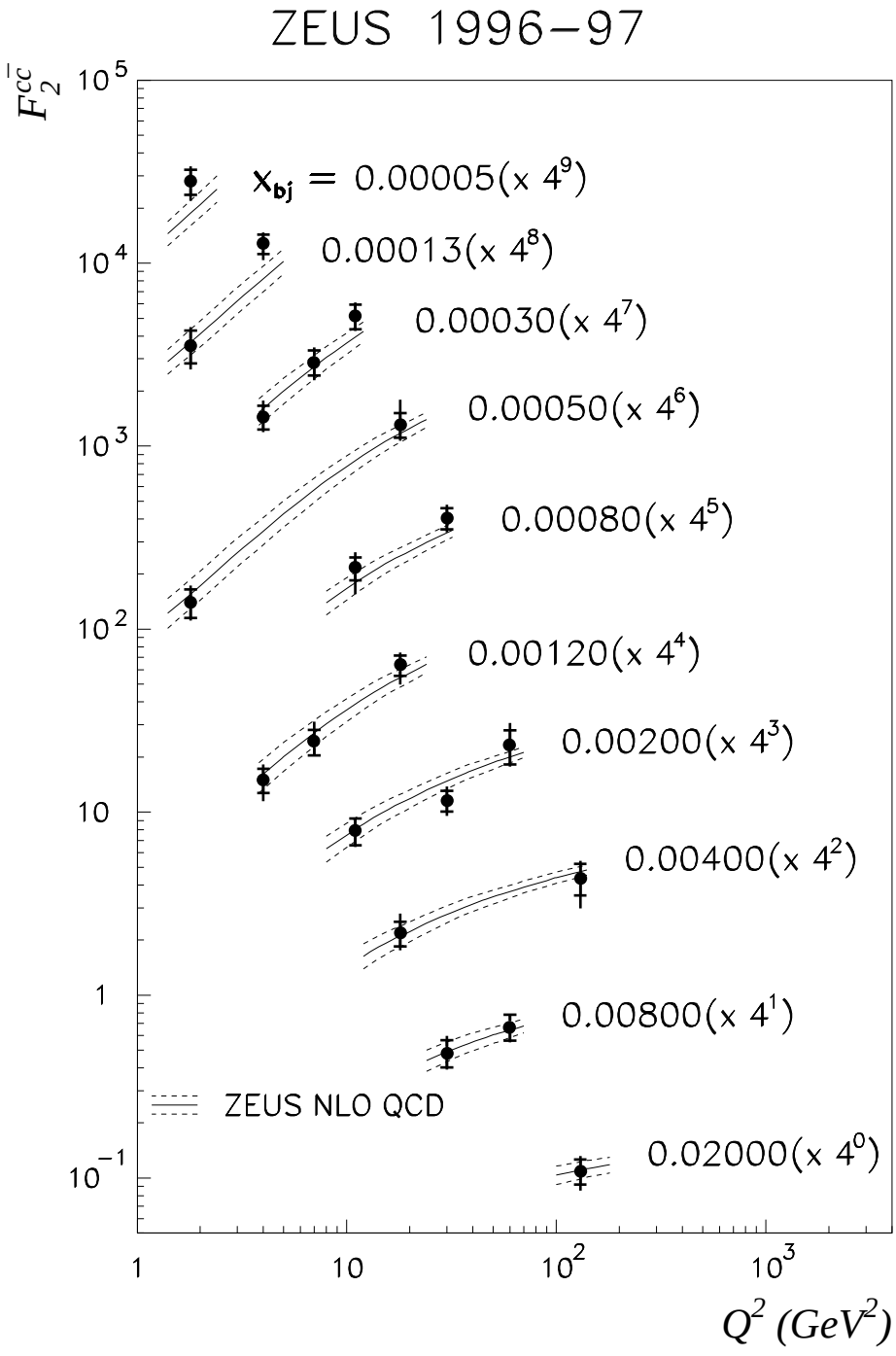

Figure 8: *The measured $F_2^{c\bar{c}}$ at x values between 0.00005 and 0.02 as a function of Q^2. The various values of x are indicated to the right of the data points. For clarity of presentation, the $F_2^{c\bar{c}}$ values have been scaled by the number shown in parentheses next to the x value. The inner error bars show the statistical uncertainty and the outer ones show the statistical and systematic uncertainties summed in quadrature. The curves correspond to the NLO QCD calculation [7, 45] using the result of the ZEUS NLO QCD fit to F_2 [41]. The solid curves correspond to the central values and the dashed curves give the uncertainty due to the parton distributions from the ZEUS NLO fit. Details of this calculation are given in the text. The overall normalization uncertainties arising from the luminosity measurement ($\pm 1.65\%$), the $D^{*\pm}$ and D^0 decay branching ratios, the charm hadronization fraction to D^{*+} ($\pm 9\%$) and the extrapolation uncertainties (see text) are not included.*

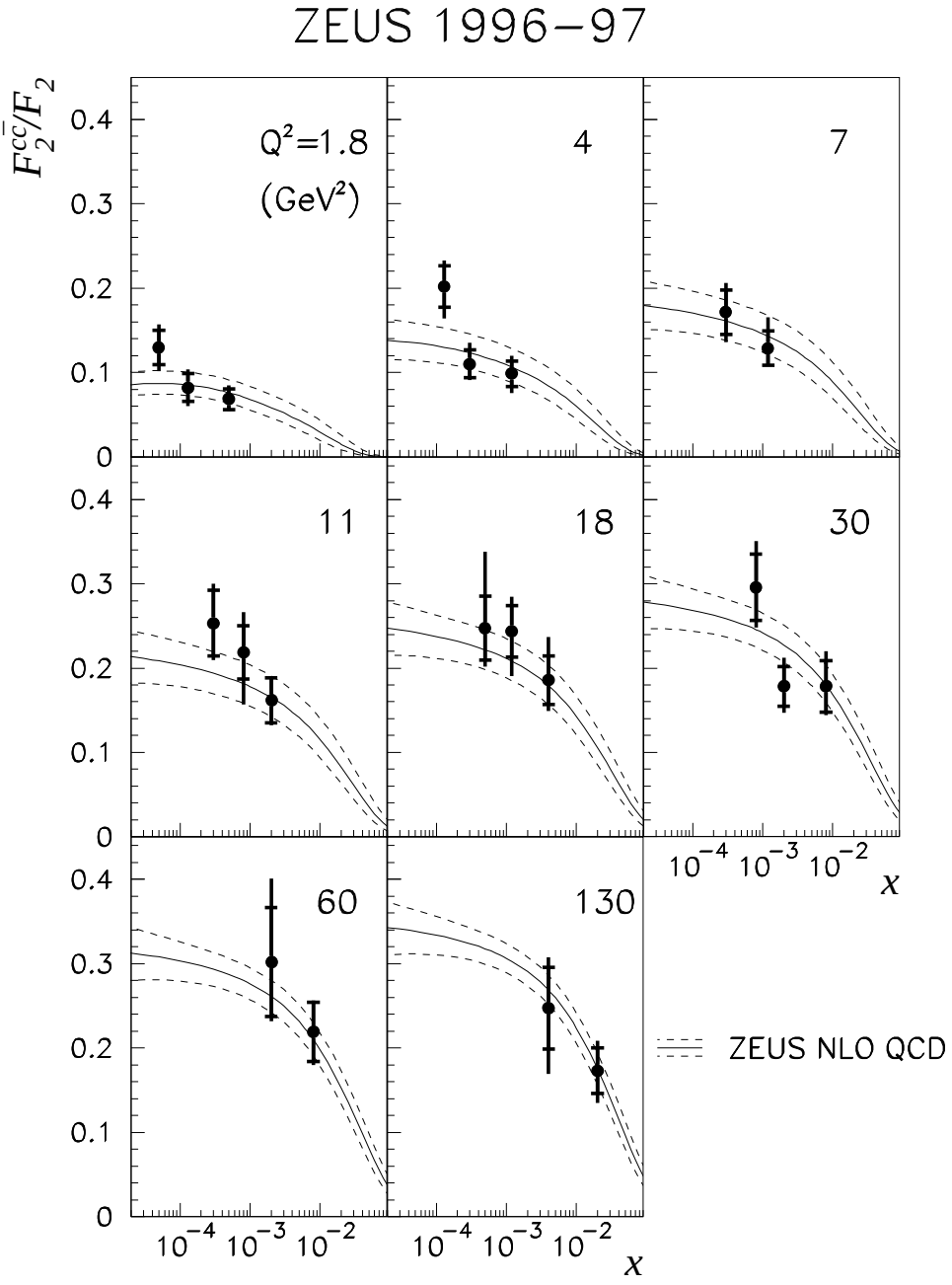

Figure 9: *The ratio of $F_2^{c\bar{c}}$ to F_2 at Q^2 values between 1.8 and 130* GeV^2 *as a function of x. The ratio is calculated using the $F_2^{c\bar{c}}$ values measured in this analysis and the ZEUS NLO QCD fit to F_2 [36]. The inner error bars show the statistical uncertainty and the outer ones show the statistical and systematic uncertainties summed in quadrature. The curves correspond to the NLO QCD calculation [7, 45] using the result of the ZEUS NLO QCD fit to F_2 [41]. The solid curves correspond to the central values and the dashed curves give the uncertainty due to the parton distributions from the ZEUS NLO fit. Details of this calculation are given in the text. The overall normalization uncertainties arising from the luminosity measurement ($\pm 1.65\%$), the $D^{*\pm}$ and D^0 decay branching ratios, the charm hadronization fraction to D^{*+} ($\pm 9\%$) and the extrapolation uncertainties (see text) are not included.*